UIC

The University of Illinois at Chicago

FINAL REPORT

Experimental and Analytical Studies
on the Kinematics of a Damage Zone During Fatigue Fracture

By

John Botsis
Department of Civil Engineering
Mechanics & Metallurgy
University of Illinois, Chicago
P.O.Box 4348, Chicago, IL 60680

DTIC
ELECTE
JUN 0 8 1992
S   D

92-14871

Prepared for :
The Air Force Office of Scientific Research
Directorate of Aerospace Sciences
Bolling Air Force Base
Washington, D.C. 20332-6448

Contract No: 89-0505

ABSTRACT

This report provides a summary of the results obtained in a research program on damage evolution before crack initiation and during slow crack propagation on a model material. First the main results on crack initiation are given. Subsequently, damage evolution within a process zone is described in some details. Results of the effects of stress rate and stress level on crack damage evolution is presented next. In appendix A, an approximate method to evaluate energy release rates due to damage growth is applied using the data on crack initiation.

Accession For	
NTIS GRA&I	☑
DTIC TAB	☐
Unannounced	☐
Justification	
By	
Distribution/	
Availability Codes	
Dist	Avail and/or Special
A-1	

SIGNIFICANT ACHIEVEMENTS

This investigation was intended to study the process of damage evolution during of crack initiation and slow crack - damage growth under low cycle fatigue conditions on a model material. The materials employed in these studies was an (amorphous polystyrene with 0.20 mm in thickness).

The results of this work showed that:

1. Damage accompanied the process of crack initiation and that of slow crack growth. Within the damage zone two patterns of damage were distinguished: A core of highly dense damage and a peripheral less dense crazes around the core zone. Crack initiation and growth occurred within the core zone.

2. In both cases of crack initiation and slow crack growth damage evolved in a self - affine manner. That is, a linear transformation related the points of equal damage at consecutive configurations of damage zone before crack initiation. Accordingly, the corresponding energy release rates may be expressed with the J and M integrals.

3. Damage density within the core of damage at crack initiation was found independent of the loading conditions, however, the pattern of the peripheral crazes was dependent on the loading conditions. Thus the large difference in crack initiation times was attributed to the shielding effect of damage around the core zone.

4. The density within the core zone remained the same during slow crack advance and equal to the density of the core zone at crack initiation.

5. The evolution of the gravity center of the core zone with energy release rate, during crack initiation, grows in a manner similar to a long crack.

Crack initiation and slow crack growth have been considered in the literature as two quite different processes. The results of the present studies, however, suggested certain similarities between these processes.

6. The effect of stress rate on crack propagation and damage evolution were investigated by conducting experiments with certain frequencies and with constant stress amplitude and mean stress level. These experimental conditions allowed for the isolation of rate and creep contribution if the kinetic data is treated as $\Delta l / \Delta t$ vs the energy release rate. For the particular loading conditions investigated, time effects were more important that the effects of load reversal.

7. The ratios of the second to the square root of the fourth moment of damage distributions along directions normal to the crack path were found independent of the loading conditions. This result may be looked upon as a similitude criterion for the particular fracture process.

TABLE OF CONTENTS

LIST OF TABLES

LIST OF FIGURES

1. INTRODUCTION

Prediction of life time of a structure under loads and the characterization of material's toughness assume a position of prominence in engineering design efforts. Consequently, their understanding and modeling are issues of central importance to engineers and material scientists alike.

In general, engineering materials fail when their load bearing capacity is compromised by the presence of defects. Upon loading, failure ensues on the microscopic level through the process of damage accumulation which results from the interaction of the pre-existing defects and the applied load. This interaction yields a macroscopic crack (crack initiation) which grows in a stable fashion until dynamic fracture. Accordingly, fatigue fracture processes are commonly divided into three phases: crack initiation, slow crack growth and dynamic (fast) fracture. The latter phase is very short in duration and thus, the time of crack initiation and that of slow crack growth account for the useful time of a structure.

The traditional approach to fatigue fracture often considers the endurance limit ΔS_0, as the resistance to crack initiation. Moreover, fracture mechanics approach to fatigue does not consider crack initiation [1,2]*. Instead, the concept of crack growth threshold is employed [3,4]. Values of the fatigue threshold signify the cyclic stress intensity factor ΔK_{th}, below which long cracks remain dormant. The corresponding ΔK_{th} is taken as a material parameter. Thus, ΔK_{th} is to crack growth what the endurance limit is to fatigue life for uncracked specimen. Because ΔS_0 is often taken as a limit on crack initiation rather than growth, ΔK_{th} can not be defined in terms of ΔS_0.

Although the study of fatigue thresholds and near threshold behavior has highlighted the effects of load history in influencing crack growth, and has provided insight into the different mechanisms of crack closure, the threshold concept has met with limited success in engineering design. This stems partly from the fact that the use of a fatigue threshold represents a conservative design criterion and partly from questions regarding its uniqueness as a material parameter [5-7].

In the literature, there has been an emphasis on crack propagation over the past several years. Since, in most cases fatigue fracture would not be expected unless a macrocrack is present, the conservative approach is to evaluate the time of propagation of a macroscopic crack using the methodologies of fracture mechanics. Thus fracture mechanics analysis fills an important role in fatigue life prediction of certain brittle material systems. However, investigations into the process of crack initiation have been limited.

Fatigue cracks are initiated at heterogeneities within the material. These heterogeneities may be pre-existent, namely, notches, grain boundaries intersecting with the free surfaces, inclusions, second phase particles, pores, etc., or are generated during the cyclic load itself. Depending on the severity of these microdefects, crack initiation may account for 20% to 80% of the total life time. Furthermore, mechanistic investigations in different materials demonstrate that damage precedes crack initiation. In metals initiation is related to intense slip processes, extrusions-intrusions and persistent slip bands (PSB) [8,9]. Excellent work has been presented concerning the behavior of cyclic deformation via dislocation kinetics and the morphology of PSB's [10-13]. Fatigue cracks initiated at inclusions or second phase particles in the case of smooth specimens have also been reported by several researchers. Observations of the same process in both notched and smooth specimens of polymers have emphasized the

---

* Numbers in brackets indicate cited literature on page 64

role of crazing in amorphous and semi - crystalline polymers [14-17]. It is believed that the accumulated damage prior to crack initiation is responsible for the early high acceleration of the average crack speed (*Figure 1.1*).

For most engineering materials, a zone of damage accompanies the process of crack initiation and slow crack growth under fatigue and creep. Damage nucleation and growth, whether in the form of crazes, microcracks, voids, homogeneous transformations, etc., is a process that absorbs energy; energy that otherwise would be available to drive the crack. Accordingly, the nature and extent of damage determine the useful life - time and toughness of the material. Therefore, the problem of damage evolution is one of critical importance. In addition, formulation of constitutive equations for damage evolution is well recognized by now to be a problem pertinent to materials' fracture.

The scope of this work was to investigate the process of damage accumulation prior to crack initiation and during slow crack - damage evolution. The material employed in the present studies was polystyrene, an amorphous polymer. Polystyrene served as a model material and was chosen because it is transparent and preserves damage patterns induced during fatigue. Thus in situ optical observations and damage evolution analyses are relatively easy to carry out. In addition, it is a well characterized material and possesses no characteristic material scales down to the molecular level. To facilitate experimental observations, the site of crack initiation was located in space by inducing a 60° -V notch onto the mid-span of the specimen edge. Therefore efforts were concentrated on observations of damage dissemination before crack initiation and during slow crack growth.

Experimental procedures and the results of the observations and analysis on crack initiation are presented in Chapter 2.

In chapter 3 a systematic characterization of damage distribution between consecutive configurations of a process zone is presented.

The effects of stress rate and stress level on crack damage evolution is discussed in Chapter 4.

Conclusions from this work are given in Chapter 5.

In Appendix A, a method for energy evaluations is briefly presented and a correlation of damage zone movements prior to crack initiation and energy release rates is given.
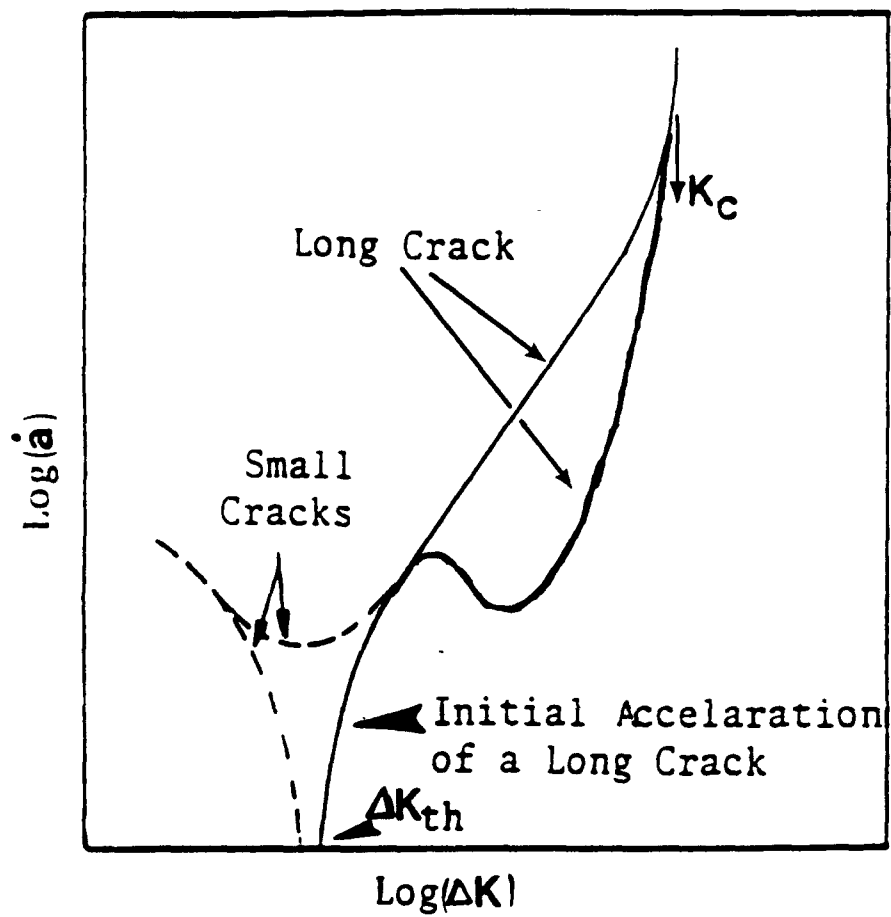
Figure 1.1   Schematic behavior of short and long cracks

2. STUDIES OF DAMAGE EVOLUTION PRIOR TO CRACK INITIATION

2.1 Experimental Procedures

2.1.1 Materials and Specimens

Commercially available amorphous polystyrene (PS) (Transilwrap, Chicago, IL) was employed in both studies of crack initiation and slow crack growth. The material was received in the form of sheets with dimensions of 200x250mm.

Strips of 150x22x0.20 mm were cut from these sheets with a razor blade and sandwiched between two pieces of acrylic of dimensions 150x21x6.5 mm.

The specimens were squared up to 150x20x0.20 mm by the use of a fly cutter on a milling machine. The speeds of the fly cutter and the longitudinal power feed of the working table which supports the specimens were 11 rotation/sec. and 0.23 mm/sec., respectively.

First, sections of about 0.25 mm thick were cut off from the block of specimens until the edges of the specimens were on the same plane. The final few cuts were in the order of 0.01 mm so that the induced damage is minimized. The block was then flipped over and the same procedure was repeated until the desired width was achieved. The machined edges were metallographically polished to a 0.5μm finish to prevent formation of edge crazes.

A double angle cutter of 60° was used to notch the specimens prior to their removal from the block. Subsequently the specimens were removed from the block and washed carefully with distilled water. Note that this procedure of specimen preparation ensures identical notch tip geometries.

Finally, the specimens were annealed in a temperature of 10°C degrees lower than T_g (glass transition temperature) for 48 hours and then allowed to slowly cool down to room temperature. Annealing was aimed at relieving any residual stresses and healing any damage formed during the cutting procedures.

2.1.2 Experimental methods

Tension - tension fatigue experiments were conducted on an Instron Testing System in laboratory environment at ambient temperature. All experiments were performed under load controlled mode with sinusoidal wave form. The specimen geometry and the wave form employed in these studies is exhibited in *Figure 2.1*.

The evolution of the damage around the notch tip was observed by means of a traveling optical microscope attached to the Instron Testing System. The fracture process was recorded using a motor driven camera which was attached to the microscope. Craze distribution was evaluated from optical micrographs of sectioned specimens (approximately 10-20μm thick) which were prepared by standard metallographic and polishing procedures. Damage density distributions were obtained by the following procedures.

Micrograph of polished sections were covered by a mesh of rectangles. In each rectangle, the number of crazes was counted. Craze density was evaluated as number per unit area or as $\rho = \frac{nbt}{abt}$ (mm^2/mm^3). ρ represents the amount of area of craze midplanes per unit volume, n is the number of intersections of crazes with the vertical test line at the respective rectangle, a and b were the height and width of a rectangle, respectively, and t is the specimen thickness [18].

To investigate the evolution of damage density prior to crack initiation, four sets of experiments were performed. The loading conditions for these experiments are shown in the following table,

	σ_{max}(MPa)	σ_{min}(MPa)	ν (Hz)
C1	8.00	2.75	0.33
C2	10.50	2.75	0.33
C3	14.30	7.00	0.33
C4	13.60	3.70	0.33

The most direct way to experimentally measure damage growth rates is by examination of sectioned samples that have been exposed to a known loading history. Thus to obtain crazing distribution prior to initiation, three sets of experiments were performed under the above experimental conditions. Each experiment was interrupted at appropriate cycle numbers. In this way damage growth was "frozen in" at various levels of development. Subsequently, the specimens were polished and the number of crazes per unit area was evaluated.

Commercially available PS is a relatively 'ductile' material. This results in a large extent of crazing during crack initiation and slow crack growth. Thus, damage within a process zone in this material is amenable to statistical treatment without the need to examine damage distribution in a large number of specimens.

One way to investigate damage evolution is to examine the contours of equal damage density at consecutive configurations. Such pointwise comparison, however, may not be appropriate because of local fluctuations in damage density. Indeed, the contours of equal damage level at each configuration obtained from different specimens exhibit noticeable fluctuation on the scale of several micrometers (*Figure 2.3*, Sec. 2.2). Therefore integral parameters, such as the inertia moments of damage within the zone, were utilized here to characterize damage distribution and its evolution.

Characterization of any distribution with the use of the inertia moments should involve comparison of a sufficiently large number of inertia moments between consecutive configurations of the distribution. In this analysis, the following even moments were evaluated for the purpose of comparing damage distributions,

$$I_o = \int\int_s \rho(x,y)dxdy$$

$$I_{2x} = \int\int_s (x-x_c)^2\rho(x,y)dxdy$$

$$I_{2y} = \int\int_s (y-y_c)^2\rho(x,y)dxdy$$

$$I_{xy} = \int\int_s (x-x_c)(y-y_c)\rho(x,y)dxdy$$

$$I_{4x} = \int\int_s (x-x_c)^4\rho(x,y)dxdy$$

$$I_{4y} = \int\int_S (y-y_c)^4 \rho(x,y)dxdy$$

$$I_{4xy} = \int\int_S (x-x_c)^2(y-y_c)^2 \rho(x,y)dxdy$$

Here I_0 is the zeroth moment and represents the total amount of crazes within a damage zone; I_{2x}, I_{2y} and I_{2xy} were the second moments with reference to the X, and Y axes, respectively; I_{4x}, I_{4y} and I_{4xy} were the respective fourth moments; S refers to the area of the damage zone. The integral signs are substituted by summation when evaluation of the inertia moments is made using the experimental data on damage density.

2.2 Results and Discussion

Upon application of the load, a core zone of crazes appears at the notch tip. While this zone increases in size, few arched crazes appear around the core zone. As time progresses, the crazes grow longer as well as new crazes nucleate and grow in and around the vicinity of the core. A series of optical micrographs taken during the experiments is shown in *Figure 2.2*. Crack initiation was defined at the instance when a crack appears at the notch tip. This event occurred relatively fast (within one fatigue cycle) and was observed through the optical microscope at a magnification of about x200.

Measurements within the damage zones at consecutive configurations yielded the contours of equal damage density, ρ (mm^2/mm^3), shown in *Figure 2.3*. Each set of contours in *Figure 2.3* reflects damage evolution under two different loading conditions. Note that, the contours of damage density have been symmetrized with respect to the bisector of the V-notch because small variations in density were observed at some points located at equal distances from the bisector. These differences were attributed to local fluctuation in damage density. Thus the density at these locations was substituted with the arithmetic mean of the respective density values. For the sake of visual clarity, the level of experimental error is not shown in *Figure 2.3*. The error in measurements of craze density far from the notch tip was about 10%. The error for the contours near the notch tip was about 15 - 20%. This was because the high craze density in the close vicinity of the crack tip limits optical microscopy which makes accurate measurements difficult.

Reproducibility of Damage Distribution prior to Crack Initiation

A complete experimental characterization of the kinematics of a damage zone requires comparison of damage distribution within the zone at different configurations. Moreover, the process of damage accumulation is a stochastic process. Thus the distributions of a sufficiently large number of identical systems should be compared at each configuration. Such an effort however, was experimentally difficult to carry out.

To check the reproducibility of damage distribution before crack initiation two experiments were performed under identical loading conditions. The experiments were interrupted shortly prior to crack initiation and at the same number of cycles (N= 12,000). The specimens were subsequently mounted and polished according to standard sectioning and polishing procedures. Damage density was measured next and the moments of inertia were evaluated. A comparison of the inertia moments of damage distribution is shown in TABLE I. This data was a sufficient indication that damage

distributions during crack initiation were reproducible. With respect to the time of crack initiation, the present studies show a difference of about 9% .

Evolution Characteristics of Damage Distribution prior to Crack Initiation

From the experimental data presented in *Figure 2.3*, the weighted center of gravity of the damage zone with reference to a coordinate system attached at the notch tip is calculated as

$$x_c = \frac{\int_{-\infty}^{+\infty} x \left(\int_{-\infty}^{+\infty} \rho(x,y) dy \right) dx}{\int_{-\infty}^{+\infty} \int_{-\infty}^{+\infty} \rho(x,y) dx dy}$$

$$y_c = \frac{\int_{-\infty}^{+\infty} y \left(\int_{-\infty}^{+\infty} \rho(x,y) dx \right) dy}{\int_{-\infty}^{+\infty} \int_{-\infty}^{+\infty} \rho(x,y) dx dy}$$

The results of these calculations are shown in *Figure 2.4*. Note that the center x_c is increasing linearly with the number of cycles (y_c was zero due to symmetry of damage distribution).

To investigate the type of transformation the damage density is undergoing during its evolution, characteristic scales along the X and Y axes can be defined as,

$$\frac{I_{2x}}{I_0} = \sigma_x^2, \qquad \frac{I_{2y}}{I_0} = \sigma_y^2$$

Since I_{2x}, I_{2y} are the second moments of the damage zone and I_0 is the zeroth moment (which expresses the total amount of crazes within the damage zone) σ_x and σ_y can be looked upon as the measurements of damage spread in the X and Y axes, respectively.

Based on these parameters, damage evolution within the damage zone can be examined by comparing the following ratios defined between i_{th} and j_{th} configurations (i= 1, 2, 3 and j=i+1),

$$\frac{\sigma_x^{(j)}}{\sigma_x^{(i)}} = \lambda_{ji}, \quad \frac{\sigma_y^{(j)}}{\sigma_y^{(i)}} = \mu_{ji} \qquad \frac{I_{4x}^{(j)}/I_0^{(j)}}{I_{4x}^{(i)}/I_0^{(i)}} = \Lambda_{ji}^4, \qquad \frac{I_{4y}^{(j)}/I_0^{(j)}}{I_{4y}^{(i)}/I_0^{(i)}} = M_{ji}^4, \qquad \frac{I_{4xy}^{(j)}/I_0^{(j)}}{I_{4xy}^{(i)}/I_0^{(i)}} = H_{ji}^4$$

The type of transformation of damage distribution between consecutive configurations was examined by comparing the following quantities:

$(\lambda_{ji}, \Lambda_{ji})$, (μ_{ji}, M_{ji}), and $(\lambda_{ji}\mu_{ji}, H_{ji}^2)$. The above defined ratios for the C1 and C2 experimental conditions are shown in TABLE II. The data in TABLE II indicates a relatively large difference in the ratios between the first and second configurations. This may be due to the fact that the system needs some time for the damage to be developed so

that statistical measurements are meaningful. However, differences between the rest of the ratios were small. This data indicates that the evolution of damage between consecutive configurations can be approximated by a linear transformation of the space variables.

It is worth pointing out that results of damage evolution within a process zone on the same material (Sec. 3.2) have shown that damage evolution can be described by a linear transformation of the space variables. These findings indicate that a similar transformation relates damage evolution before crack initiation and consecutive crack growth.

The evolution of an average damage density $<\rho> = \Sigma/S$, where Σ is the total number of crazes within the zone and S is the area of the zone with normalized cycle number is shown in *Figure 2.5*. (Because of the large difference in the cycles to crack initiation between the different experimental conditions, C1: 300,000 cycles, C2: 27,000, C3: 19,500, the number of cycles has been normalized with the respective cycle number at initiation in order to clearly see the trend of $<\rho>$). Note that the dependencies of $<\rho>$ are of a damping character. That is, initially the rate of damage density was fast, but gradually decreased. Moreover, the data in *Figure 2.5* shows that while the rates of damage accumulation were different, craze density $<\rho>$, at crack initiation were 40,000, 44,200 and 47,000 mm^{-2}, respectively. Note that the error between the extreme values of these densities was 16% while the largest difference from the mean was about 10%. Thus one may be led to consider the value of $<\rho>$ as being independent of the loading conditions at crack initiation. This would be realistic if the density within the zone was homogeneously distributed. However, the results of these studies clearly indicate that damage was not homogeneously distributed. Accordingly, an average quantity like $<\rho>$ may not be indicative of the crack initiation event.

On the other hand, crack initiation as well as crack growth (Sec. 3.2, *Figures 3.7 and 3.8*) occur within an area where damage was highly localized (*Figures 2.6 and 2.7*). Within the resolution of the experimental measurements, damage density at the notch tip was about 1,300 mm^2/mm^3. Similar values of damage density has been obtained in the close proximity of the crack tip during slow crack damage growth (Sec. 3.2). Whether this density is a material parameter and a criterion for crack initiation and subsequent crack growth should be further investigated both experimentally as well as analytically.

The optical micrographs in *Figures 2.6* and *2.7* bring out an important observation: While the density at the notch tip was practically independent of the loading conditions, the number to crack initiation were drastically different, 9,450 and 19,500 cycles, respectively. Moreover, damage dissemination around the core zone was quite different (*Figures 2.6* and *2.7*). Thus, the difference in the cycle number at crack initiation may be attributed to the role of damage around the core zone. In the second case the surrounding damage plays a shielding role which gives rise to longer time to crack initiation.

It was stated earlier that a small crack was observed at the notch tip in about one cycle. This event was associated with the crack initiation. An accurate initial crack size, however, was difficult to detect with the use of standard optical observations during the fatigue test. To evaluate an initial crack size, the crack was allowed to grow after initiation. Next, the specimen was pulled to fracture and the fracture surface was observed under a microscope in order to examine its morphology. A typical micrograph of a fracture surface near the notch tip is shown in *Figure 2.8*.

The morphology of the fracture surface suggested that the crack front was not straight. Instead, crack grows more in the middle than at the edges of the specimen surface. Based on the observed morphology, an average crack size at initiation was about 35 μm.

TABLE I   INERTIA MOMENTS FOR TWO CONFIGURATIONS OF DAMAGE BEFORE CRACK INITIATION*

Configuration	1	2	1	2
	Reference to crack tip		Reference to gravity center	
x_c(mm)	5.5×10^{-2}	5.2×10^{-2}		
y_c(mm)	0.0	0.0		
I_o (number)	732	689		
I_{2x}(mm^2)	0.28×10	0.25×10	0.65	0.63
I_{2y}(mm^2)	0.46	0.42	0.46	0.42
I_{4x}(mm^4)	0.20×10^{-1}	0.18×10^{-1}	0.11×10^{-2}	0.11×10^{-2}
I_{4y}(mm^4)	0.57×10^{-3}	0.52×10^{-3}	0.57×10^{-3}	0.52×10^{-3}
I_{4xy}(mm^4)	0.21×10^{-2}	0.18×10^{-2}	0.40×10^{-3}	0.39×10^{-3}
I_{xy}(mm^2)	0.0	0.0	0.0	0.0

Loading Conditions C2

TABLE II   MOMENT RATIO OF DAMAGE DISTRIBUTION AT CONSECUTIVE CONFIGURATIONS BEFORE CRACK INITIATION

Condition C1

$\lambda_{21}=1.20$	$\Lambda_{21}=1.15$	$\mu_{21}=1.02$	$M_{21}=1.02$	$\lambda_{21}\mu_{21}=1.22$	$H^2_{21}=1.15$
$\lambda_{32}=1.57$	$\Lambda_{32}=1.55$	$\mu_{32}=1.30$	$M_{32}=1.34$	$\lambda_{32}\mu_{32}=2.04$	$H^2_{32}=2.07$
$\lambda_{43}=1.43$	$\Lambda_{43}=1.46$	$\mu_{43}=1.30$	$M_{43}=1.30$	$\lambda_{43}\mu_{43}=1.86$	$H^2_{43}=1.90$

Condition C2

$\lambda_{21}=1.11$	$\Lambda_{21}=1.10$	$\mu_{21}=1.22$	$M_{21}=1.15$	$\lambda_{21}\mu_{21}=1.35$	$H^2_{21}=1.28$
$\lambda_{32}=1.17$	$\Lambda_{32}=1.17$	$\mu_{32}=1.23$	$M_{32}=1.23$	$\lambda_{32}\mu_{32}=1.44$	$H^2_{32}=1.41$
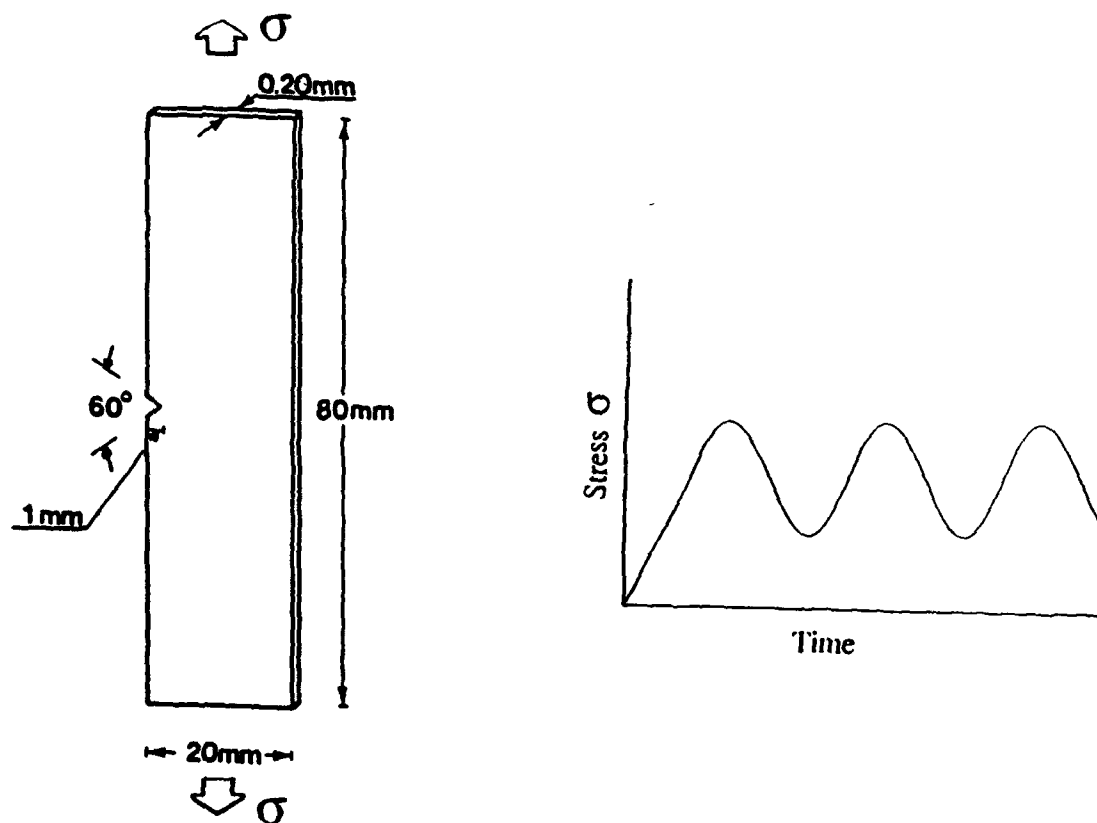
Figure 2.1   Specimen geometry and the wave form of loading

Cycles: 0

Cycles: 130

Cycles: 250

Cycles: 23,040

Cycles   38,760

Cycles: 39,430
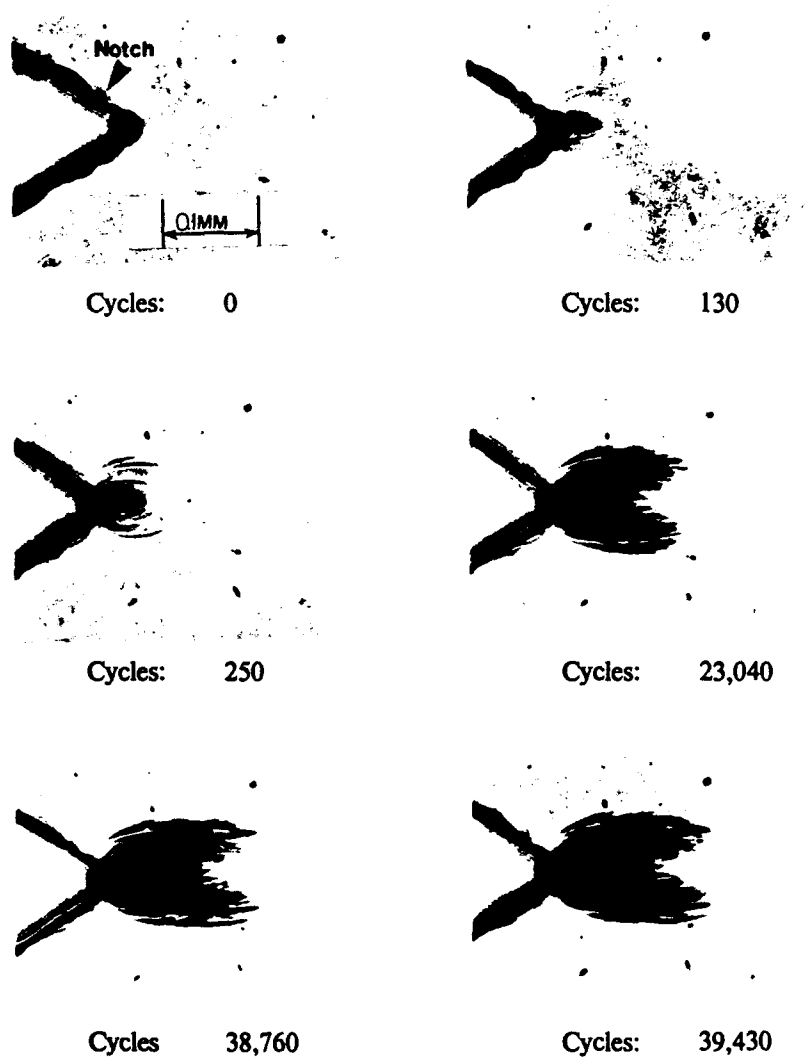
Figure 2.2   Series of optical micrographs before crack initiation
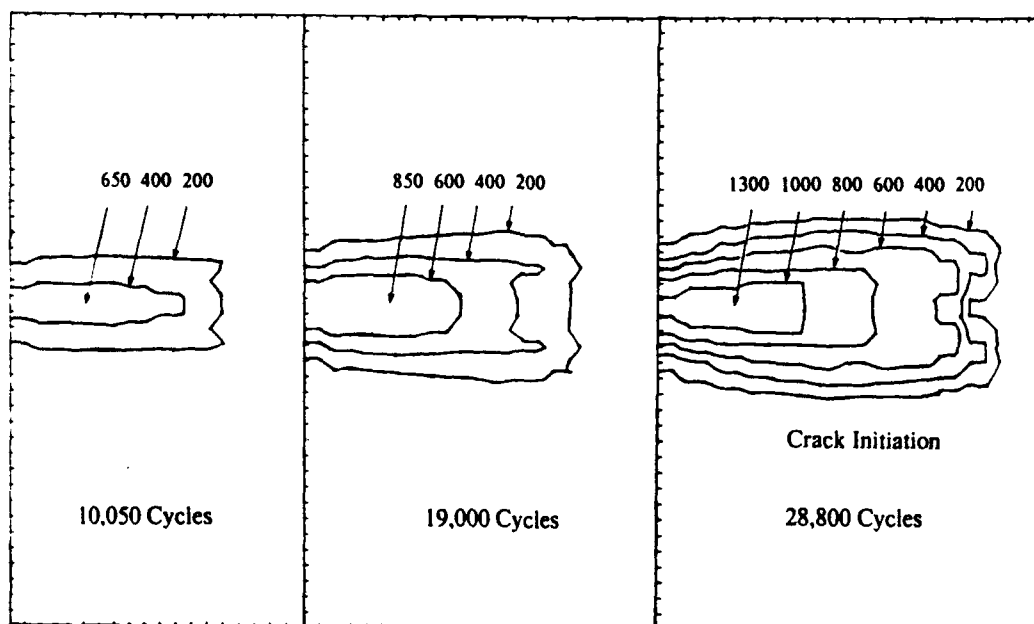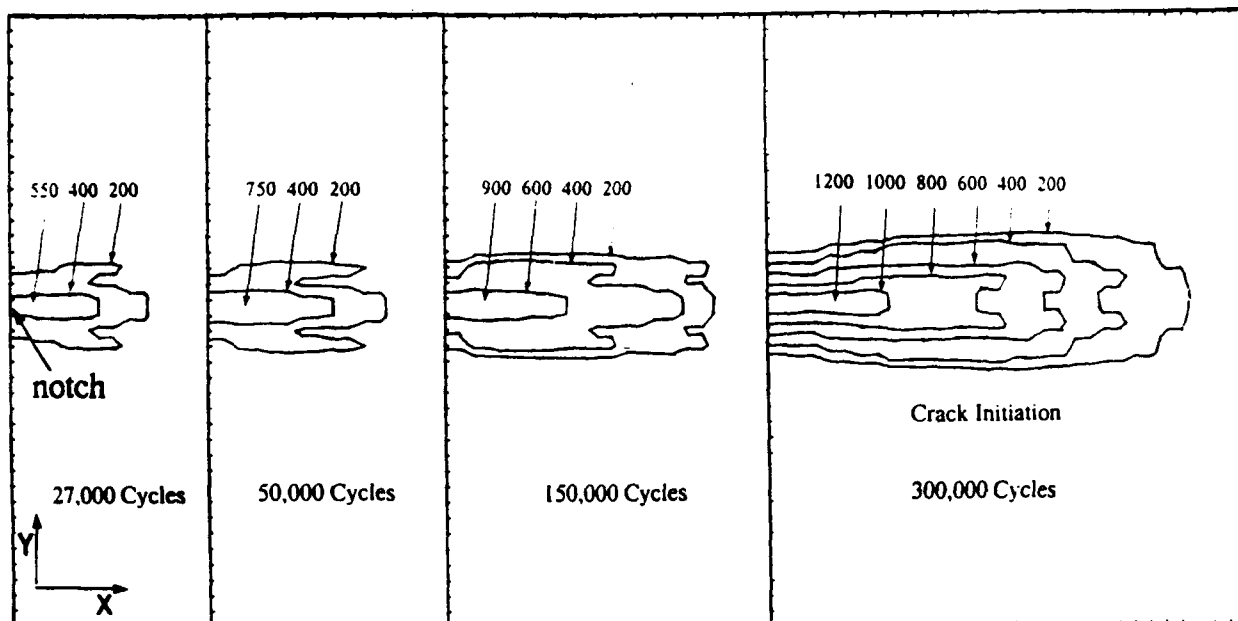
Figure 2.3 Contours of equal damage density withina damage zone before crack initiation for two loading conditions, C1, C2
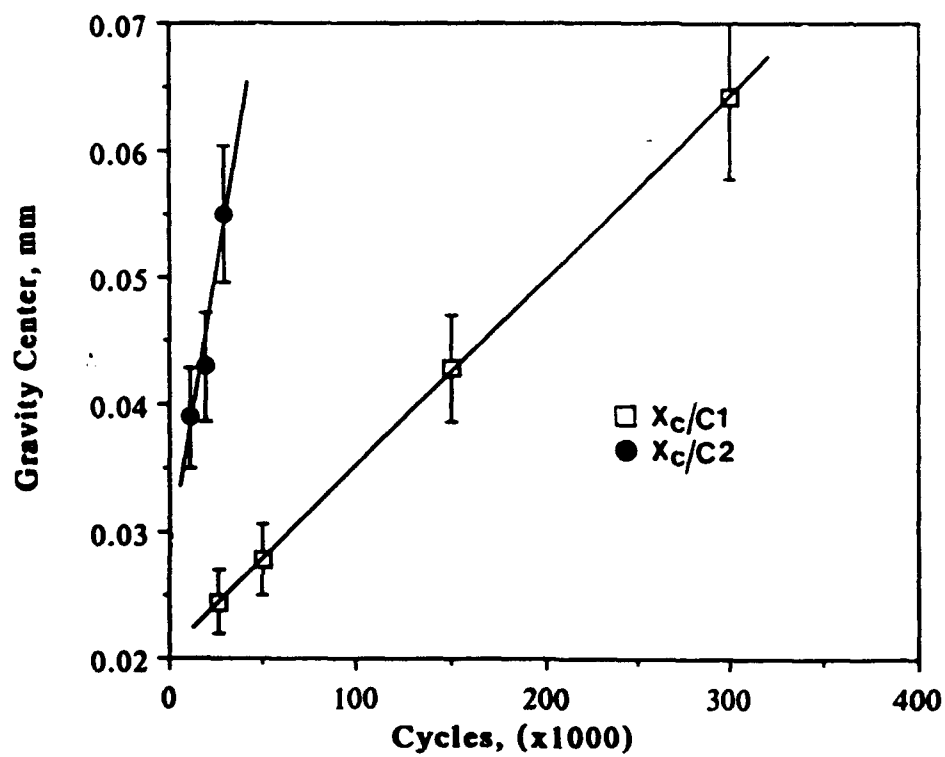
Figure 2.4   The gravity center of a damage zone
as a function of cycle number
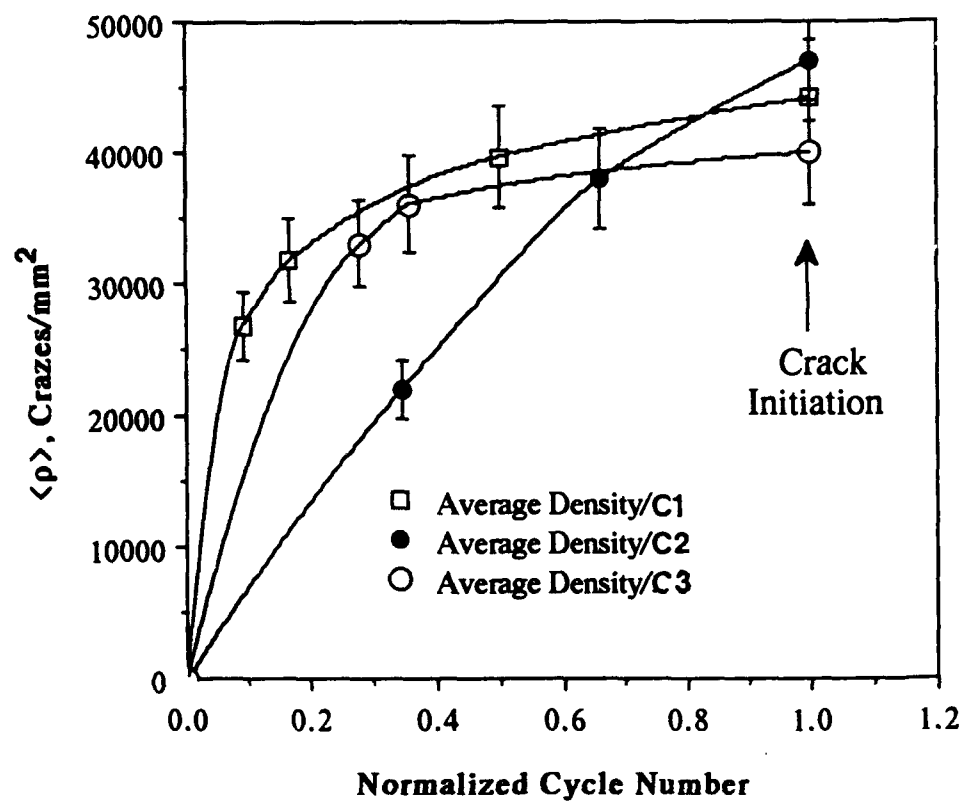
Figure 2.5 Evolution of an average damage density during crack initiation for three loading conditions

Figure 2.6   Optical micrographs showing damage distribution at crack initiation for conditions C3
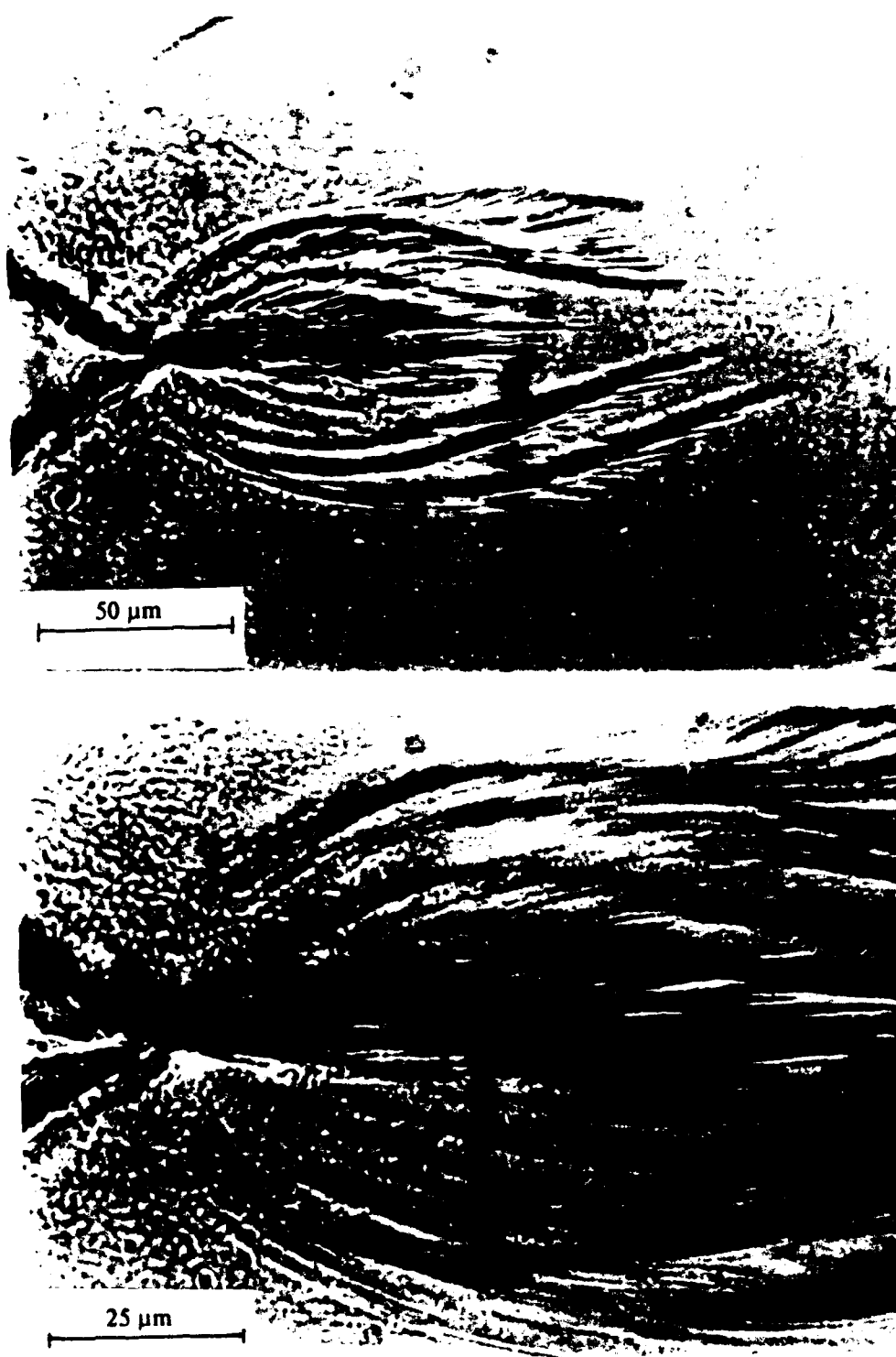
Figure 2.7   Optical micrographs showing damage distribution at crack initiation for conditions C4
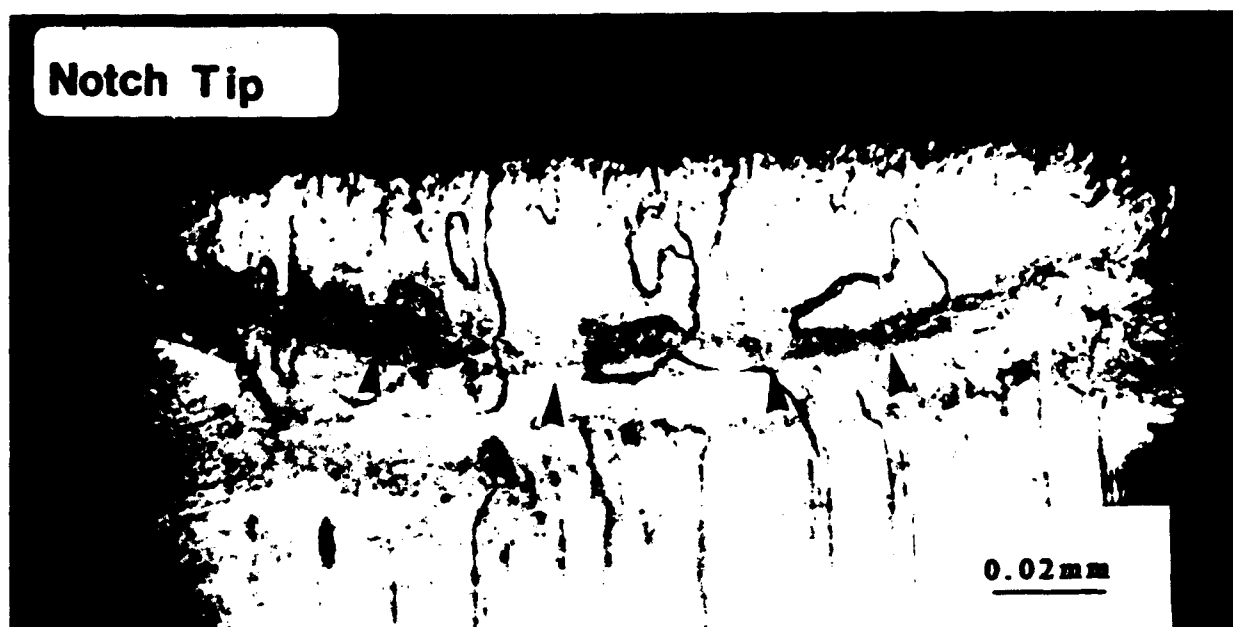
Figure 2.8   Morphology of the fracture surface at crack initiation. Arrows point at the crack front at initiation (crack grows from top to bottom)

3. STUDIES OF DAMAGE DISTRIBUTION DURING SLOW CRACK PROPAGATION

3.1 Experimental Methods

Tension-tension fatigue experiments were conducted on a 2.5 Kip capacity servohydraulic two actuator Instron Testing System in a laboratory atmosphere using a sinusoidal wave form loading function (*Figure 2.1*) at a frequency of 1.11 Hz, σ_{max}=14.7MPa and a load ratio of 0.28.

An experiment was conducted initially, in order to record the crack growth kinetics and obtain the interval of stable crack - damage evolution. Utilizing a method to identify the critical crack length l_c, which is described in [14], the resulting value of l_c was 7.5 mm.

Beyond a crack length of about 6 mm the crack grows relatively fast and with large jumps. This makes a controlled interruption of the experiment difficult. Thus analyses of damage distribution within process zones was performed on configurations with crack lengths less than 5.5 mm.

The kinematics of the process zone were investigated by comparing crazing distribution at six different configurations. Accordingly, six experiments were performed and interrupted when the respective crack lengths reach the values of 2.2, 3.6, 3.8, 4.5, 4.8 and 5.5 mm.

Crack propagation and the evolution of the damage surrounding the crack were observed by means of a Questar long range microscope. The fracture process was recorded using a Hamamatsu video system (recording speed=30 frames/s) which was attached to the microscope. The craze distribution was evaluated from optical micrographs of sectioned specimens (approximately 10-20µm thick) which were prepared by standard metallographic and polishing procedures.

It is reported in reference [18] that during rectilinear CL propagation in PS, crazing was uniformly distributed in the thickness direction. Therefore sections parallel to the plane of the specimen adequately represent craze distribution within a process zone. In addition, no changes in orientation of crazes observed during CL propagation. Accordingly, damage was characterized as the area of craze middle plane per unit test volume, ρ [mm^2/mm^3].

A typical micrograph of polished sections of a process zone is shown in *Figure 3.2*. From these micrographs, the distributions of damage density within the process zones at six successive configurations were obtained by the following procedures.

The micrographs were covered by a mesh of rectangles whose size is approximately one order of the magnitude less than the area interested. In each rectangle, the number of intersections of the crazes with a vertical test line was counted. Craze density ρ was

evaluated as $\rho = \dfrac{nbt}{abt}$, where ρ (mm^2/mm^3) represents the amount of area of craze midplanes per unit volume, n is the number of intersections of crazes with the vertical test line at the respective rectangle, a and b are the height and width of a rectangle, respectively, and t is the specimen thickness.

3.2 Results and Discussion

A typical configuration of a crack - damage system, a crack layer (CL), in PS is illustrated in *Figure 3.1* [18,19]. The process and wake zones are distinguished by

damage growth rate $\dot{\rho}$; it vanishes in the wake zone, i.e. $\dot{\rho} = 0$ with $\rho > 0$, and has a

positive value in the process zone, i.e. $\dot{\rho} > 0$ with $\rho > 0$. The process zone is viewed as an area where intense damage growth occurs before crack growth. The wake zone is viewed as an area behind the crack tip where stress relaxation has just taken place because of crack advance. Parameters l_a and w represent characteristic length and width of the process zone.

The evolution of process zone width w, length l_a, and their ratio w/l_a as a function of crack length is shown in *Figure 3.3*. Note that while both w and l_a increase with the crack length their ratio decreases and fluctuates with the increase in crack length.

Three typical CL systems are shown in *Figure 3.4*. Following the procedures outlined in the previous section, three dimension distribution of craze density within the process zone can be constructed for each configuration. Such distributions for the three process zone are shown in *Figure 3.5*. Note that damage density reaches a maximum in the close proximity of the crack tip.

In a study reported in reference [20], the kinematic parameters were deduced from the evolution of the characteristic dimensions w and l_a of the process zone. These results were only qualitative since damage distribution within the process zone was not homogeneous (*Figure 3.5*). Therefore the kinematics of a process zone should be obtained from analysis of damage distribution at different configurations.

Reproducibility of Damage Distribution within a Process Zone

A complete experimental characterization of the kinematics of a process zone requires comparison of damage distribution within the zone at different configurations. Moreover, the process of a CL growth is, in fact, a stochastic process. Thus the distributions of a sufficiently large number of identical systems should be compared at each configuration. Such an effort however, was experimentally difficult to carry out. Independent studies have shown that in PS the macroscopic behavior of a CL is well reproducible. In addition, analysis of craze distribution along the trailing edge of the process zone (*Figure 3.1*) in specimens fatigued under the same loading conditions has shown that, at identical crack lengths, the distributions were the same.

In addition, damage distribution within a process zone was found practically similar. This was achieved by performing two fatigue experiments under the experimental conditions described in Sec. 3.1. The crack lengths and the characteristic sizes of the process zone in these experiments were $l = 3.00$ mm, $l_a = 0.25$ mm, w= 0.14 mm and l=3.0 mm, l_a= 0.14 mm, w= 0.15 mm and the number of cycles to grow the CL in these experiments were N= 41,020 and 39,720 cycles, respectively.

The polished sections of the process zones pertaining to the aforementioned experiments are shown in *Figure 3.6*. The respective contours of equal damage density are displayed in *Figure 3.7*. The data presented in *Figure 3.7* indicates that the damage distribution within a process zone was reproducible. A quantitative comparison of these distributions through the moments of inertia (Sec. 2.1.2) is presented in the following.

Evolution Characteristics of Damage Distribution within a Process Zone

Measurements within the process zones at six configurations (Sec. 3.1) yielded the contours of equal level of damage density ρ, shown in *Figure 3.8* (polygonal lines). Using non-linear regression analysis, the contours were approximated by ellipses (smooth lines, *Figure 3.8*). Note that for the sake of visual clarity, the level of experimental error

is not shown in *Figure 3.8*. The error of damage density for the contours with $\rho = 300$, 600, 900, and 1200 mm^2/mm^3 was about 15%. The error for the contours with the highest damage density ($\rho \sim 1500$ mm^2/mm^3) was about ~25%. This is because the high craze density in the close vicinity of the crack tip limits optical microscopy which makes accurate measurements difficult.

From the experimental data presented in *Figure 3.8*, the weighted center of gravity of the process zone (x_c, y_c) with reference to a coordinate system attached at the crack tip was calculated. The results of these calculations (*Figure 3.9*) indicates that the distance of the gravity center from the crack tip x_c was a linearly increasing function of crack length. The quantity $y_c = 0$, since the damage distribution was symmetric about the y axis. Moreover, it is interesting to note that the gravity center was located at a distance of $l_a/3$ from the crack tip (*Figure 3.10*).

Figure 3.11 shows the evolution of speeds of the crack length l and the gravity center $L = l + x_c$, as a function of crack length. Note that both l and L practically coincide since the value of x_c was small as compared to the respective crack length.

Inertia Moments Analysis of Damage Distribution

The type of transformation of damage between consecutive configurations was examined with the use of the moments of inertia (see Sec. 2.1.2). Values of the zeroth, second and fourth moments around the X and Y axes attached at the gravity center of the process zone are shown in TABLE III. Accordingly, the following ratios were compared:

$\lambda_{ji}^4 / \Lambda_{ji}^4$, μ_{ji}^4 / M_{ji}^4, and $\lambda_{ji}^2 \mu_{ji}^2 / H_{ji}^4$ (i= 1,...5 and i<j≤6) The data in *Figure 3.12* demonstrates that all these ratios were approximately equal to 1. These equalities indicate that the evolution of damage between consecutive configurations can be approximated by a linear transformation of the space variables.

Figure 3.13 demonstrates the evolution of $\sigma_x^{(j)}/\sigma_x^{(1)}$ (*Figure 3.13*a) and $\sigma_y^{(j)}/\sigma_y^{(1)}$ (*Figure 3.13*b), with j=1,...6; $\sigma_x^{(1)}$, $\sigma_y^{(1)}$ are the damage spreads in X and Y directions at configuration 1. The data in *Figure 3.13* shows that the ratios of $\sigma_x^{(j)}/\sigma_x^{(1)}$ and $\sigma_y^{(j)}/\sigma_y^{(1)}$ are linear functions of crack length. The increase of these ratios with the crack length shows that crack growth was accompanied by both translation and deformation of the process zone. Rotation of the zone was not observed because of the symmetries of specimen geometry and applied load. These results support the assumption regarding the kinematics of a process zone [19,21].

The reproducibility of damage distribution within a process zone was also examined by comparing the inertia moments of the respective distributions. Values of the second and fourth moments of the damage within the two process zones presented in *Figure 3.7* are given in TABLE IV. These data show that damage distributions within process zones, grown under identical loading conditions and at the same crack length, have practically the same zeroth, second and fourth moments. These data was a sufficient indication that damage distribution, under the specific loading condition, material and specimen geometry, was reproducible.

Contour Analysis of Damage Distribution

It was stated earlier that a pointwise comparison of damage density between consecutive configurations may not be appropriate because of the fluctuations in damage density. Nevertheless, it is of interest to examine the results regarding the transformation of damage distribution by investigating the transformation of contours with equal damage density between consecutive configurations. Below, an analysis is presented based the contours with equal damage density. Subsequently, a comparison of the results from the inertia moments analysis and from contours analysis is given.

By non-linear regression, it is shown that the contours can well be approximated by ellipses (smooth lines in *Figure 3.8*),

$$\frac{(x-c)^2}{a^2} + \frac{y^2}{b^2} = 1$$

where x, y are the coordinates of a point on the elliptical contour and a, b, c are the major, minor axis and the center of the respective ellipse.

A schematic diagram of contours with equal damage density ρ_{ik} at three consecutive configurations is shown in *Figure 3.14*. Throughout this discussion, the indices k = 1,...,5 and i = 1,...,6 refer to the k_{th} contour in the i_{th} configuration.

In order to investigate the transformation of contours with equal damage density, the following ratios were examined,

$$\alpha_{ji} = \frac{a_{kj}+c_{kj}}{a_{ki}+c_{ki}} \qquad \beta_{ji} = \frac{b_{kj}}{b_{ki}}$$

where j = i + 1. Values of α_{ji} and β_{ji}, corresponding to the k_{th} contours of equal damage density between successive configurations i and j, are shown in *Figure 3.15 (a)* and *(b)*, respectively.

Within experimental error, the data in *Figure 3.15* indicates that both α_{ij} and β_{ji} keep constant for all of contours (k=1,...,5). These results was an additional evidence that crazing density transform linearly from configuration to configuration.

Note that in the contour analysis there are five contours of equal damage density for each configuration and there are five values of α_{ji} and β_{ji} which were compared between two consecutive configurations (*Figure 3.15*). However, through the inertia moments analysis, single values of λ_{ji} and μ_{ji} between configurations were obtained. To compare the data, shown in *Figure 3.15*, with the results obtained from the inertia moments analysis, the following average values of $<\alpha_{ij}>$ and $<\beta_{ji}>$ were defined,

$$<\alpha_{ji}> = \frac{1}{n}\sum_{k=1}^{n} \alpha_{ji}^{(k)} \qquad <\beta_{ji}> = \frac{1}{n}\sum_{k=1}^{n} \beta_{ji}^{(k)}$$

Here n=5, is the number of contours of each configuration. The ratios of $<\alpha_{ji}>/\lambda_{ji}$ and $<\beta_{ji}>/\mu_{ji}$ shown in *Figure 3.16* demonstrate that the contour and inertia moment analyses yielded practically the same results.

Kinematics of Damage Evolution

The analysis presented in the previous sections suggested that the transformation of damage distribution can be approximated by a linear function of the space variables. These results support the kinematic assumption adopted in [19,20].

According to the CL model [19], the rate of damage evolution at a point $\mathbf{x}$ within an process zone in the coordinate system attached to the gravity center of the process zone is,

$$\dot{\rho}(\mathbf{x}) = \partial_t\rho(\mathbf{x}) - V_m(\mathbf{x})\partial_m\rho(\mathbf{x}) \qquad (4.1)$$

where $\mathbf{x}$ is the position vector, $V_m(\mathbf{x})$ is the transformation velocity of the corresponding point within the process zone and ∂ stands for partial derivative. Reference [19] has taken the partial time derivative of damage density equal to zero by the self-similarity hypothesis of damage evolution. This assumption implies that a critical level of damage around the crack tip is maintained constant during crack propagation. Experimental results shown in *Figure 3.17*, [18], and the results of the present studies (*Figure 3.5*) were in favor of this hypothesis. Thus Eq. (4.1) becomes,

$$\dot{\rho}=-V_m(\mathbf{x})\partial_m\rho(\mathbf{x}) \qquad (4.2)$$

Since the transformation of a process zone is affine, the velocity $V_i(x)$ can be approximated by the first two terms of Taylor series around the gravity center,

$$V_m(\mathbf{x}) = V_m(0)+V_{m,n}(\mathbf{x})x_n \qquad (4.3)$$

The first term on the right hand side represents the rigid translation of the process zone and the second term represents the rotation (anti-symmetric part of $V_{m,n}$) and the deformation (symmetric part of $V_{m,n}$) which in turn can be decomposed into isotropic expansion and homogeneous distortion of the process zone.

The preceding experimental results and analysis have indicated that damage evolution can be approximated by a linear function of the space variables. Accordingly, the velocity $V_m(\mathbf{x})$ could be expressed expressed in terms of the transformation coefficients λ_{ji} and μ_{ji}. Moreover, the rates of expansion and distortion may be evaluated in terms of the coefficients of transformation. This is shown next.

The transformation matrix of points with equal damage density between configuration i, j is,

$$D = \begin{bmatrix} \lambda_{ji} & 0 \\ 0 & \mu_{ji} \end{bmatrix} \qquad (4.4)$$

which can be rewritten as,

$$D = \begin{bmatrix} 1+\Delta\lambda_{ji} & 0 \\ 0 & 1+\Delta\mu_{ji} \end{bmatrix} = I+\Delta D \qquad (4.5)$$

where I is the identity matrix and,

$$\Delta D = \begin{bmatrix} \Delta\lambda_{ji} & 0 \\ 0 & \Delta\mu_{ji} \end{bmatrix} \qquad (4.6)$$

Thus the displacement field can be expressed as,

$$\begin{bmatrix} x+\Delta x \\ y+\Delta y \end{bmatrix} = \begin{bmatrix} 1+\Delta\lambda_{ji} & 0 \\ 0 & 1+\Delta\mu_{ji} \end{bmatrix} \begin{bmatrix} x \\ y \end{bmatrix} + \begin{bmatrix} \Delta L \\ 0 \end{bmatrix} \qquad (4.7)$$

where, $\Delta L = \Delta l + \Delta x_c$, l is the crack length and x_c is the x-coordinate of gravity center. The Eq. (4.7) can be rewritten as,

$$\begin{bmatrix} \Delta x \\ \Delta y \end{bmatrix} = \begin{bmatrix} \Delta\lambda_{ji} & 0 \\ 0 & \Delta\mu_{ji} \end{bmatrix} \begin{bmatrix} x \\ y \end{bmatrix} + \begin{bmatrix} \Delta L \\ 0 \end{bmatrix} \qquad (4.8)$$

Dividing both sides by the increment of loading cycle number, it is obtained

$$\frac{1}{\Delta N} \begin{bmatrix} \Delta x \\ \Delta y \end{bmatrix} = \frac{1}{\Delta N} \begin{bmatrix} \Delta L \\ 0 \end{bmatrix} + \frac{1}{\Delta N} \begin{bmatrix} \Delta\lambda_{ji} & 0 \\ 0 & \Delta\mu_{ji} \end{bmatrix} \begin{bmatrix} x \\ y \end{bmatrix} \qquad (4.9)$$

or

$$\begin{bmatrix} V_1 \\ V_2 \end{bmatrix} = \begin{bmatrix} \dot{L} \\ 0 \end{bmatrix} + \begin{bmatrix} \dot{\lambda}_{ji} & 0 \\ 0 & \dot{\mu}_{ji} \end{bmatrix} \begin{bmatrix} x \\ y \end{bmatrix} \qquad (4.10)$$

where V_1 and V_2 are the components of the transformation velocity.
Comparison of Eq. (4.10) and Eq. (4.3) results in,

$$V_m(x) = \begin{bmatrix} V_1 \\ V_2 \end{bmatrix} \qquad (4.11a)$$

$$V_m(0) = \begin{bmatrix} \dot{L} \\ 0 \end{bmatrix} \qquad (4.11b)$$

$$V_{m,n}(x) = \begin{bmatrix} \dot{\lambda}_{ji} & 0 \\ 0 & \dot{\mu}_{ji} \end{bmatrix} \qquad (4.11c)$$

The rates of expansion and distortion can be obtained by the following decomposition,

$$\begin{bmatrix} \dot{\lambda}_{ji} & 0 \\ 0 & \dot{\mu}_{ji} \end{bmatrix} = \frac{1}{2} \begin{bmatrix} \dot{\lambda}_{ji} + \dot{\mu}_{ji} & 0 \\ 0 & \dot{\lambda}_{ji} + \dot{\mu}_{ji} \end{bmatrix} - \frac{1}{2} \begin{bmatrix} -\dot{\lambda}_{ji} + \dot{\mu}_{ji} & 0 \\ 0 & \dot{\lambda}_{ji} - \dot{\mu}_{ji} \end{bmatrix} \tag{4.12}$$

where the first matrix in the right hand side is the rate of expansion $\dot{e}$ and the absolute value of the second term is the rate of distortion $\dot{d}$ of the process zone. The evolution of $\dot{e}$ and $\dot{d}$ with crack length is shown in *Figure 3.18a* and *3.18b*, respectively.

The data in *Figure 3.11* and *3.18* indicate that the evolution of damage distribution, or for that matter, the evolution of process zone can be described by rigid translation (*Figure 3.11*), and isotropic expansion the homogeneous distortion being relatively small (*Figure 3.17*). Accordingly, the corresponding energy release rates being given by the J_1, M, and N_{ij} integrals [19,21].

Integral Characteristics of Damage Distribution

In this section it will be shown that some integral parameters of damage distribution remain constants as a result of the affine transformation.

The data in *Figure 3.3* indicates that he evolutions of the width w and the length l_a (*Figure 3.3*) of an process zone could be described as linear functions of crack length l,

$$l_a(l) = m_1 l + b_1 \tag{4.13}$$

$$w(l) = m_2 l + b_2 \tag{4.14}$$

where m_1, m_2, b_1 and b_2 are load history dependent constants. They can be evaluated by regression analysis of the experimental data.

Inasmuch as the transformation of damage within process zone was linear, damage density between consecutive configurations i and j is related by,

$$\rho_i(\mathbf{x}) = \rho_j(\mathbf{D}\mathbf{x}) \tag{4.15}$$

where the coordinate system refers to the gravity center of the process zone.

With the use of Eq. (4.15), it can be proven that an average density along the trailing edge, $<\rho_W>$, as well as within of the process zone, $<\rho_A>$, remain constant during CL propagation.

Let $\rho_W^{(1)}$ and $\rho_W^{(2)}$ be the damage densities at corresponding points along the trailing edges between consecutive configurations. From Eq. (4.15) there results,

$$\rho_W^{(1)}(y) = \rho_W^{(2)}(\mu_{21}y) \tag{4.16}$$

Assuming that the damage distribution along a trailing edge can be approximated by a normal distribution (see *Figure 3.19*), the quantities $\rho_w^{(1)}$ and $\rho_w^{(2)}$ can be expressed as,

$$<\rho_w^{(1)}> = \frac{\displaystyle\int_{-\infty}^{+\infty} \rho_w^{(1)}(y)dy}{6\sigma_y^{(1)}} \qquad (4.17a)$$

$$<\rho_w^{(2)}> = \frac{\displaystyle\int_{-\infty}^{+\infty} \rho_w^{(2)}(y)dy}{6\sigma_y^{(2)}} \qquad (4.17b)$$

where $\sigma_y^{(i)}$ (i = 1,2) is the standard deviation of the damage distribution (note that the width of the process zone was approximated by $6\sigma_y$) and ,

$$\sigma_y^{(i)} = \left[\frac{\displaystyle\int_{-\infty}^{+\infty} y^2\rho_w^{(i)}(y)dy}{\displaystyle\int_{-\infty}^{+\infty} \rho_w^{(i)}(y)dy} \right]^{1/2} \qquad (4.18)$$

Using Eqs (4.15) and (4.16),

$$\sigma_y^{(1)} = \left[\frac{\dfrac{1}{\mu_{21}^3}\displaystyle\int_{-\infty}^{+\infty} (\mu_{21}y)^2\rho_w^{(2)}(\mu_{21}y)d(\mu_{21}y)}{\dfrac{1}{\mu_{21}}\displaystyle\int_{-\infty}^{+\infty} \rho_w^{(2)}(\mu_{21}y)d(\mu_{21}y)} \right]^{1/2} \qquad (4.19)$$

Substituting $\mu_{21}y = \eta$,

$$\sigma_y^{(1)} = \frac{1}{\mu_{21}} \left[\frac{\int_{-\infty}^{+\infty} (\eta)^2 \rho_w^{(2)}(\eta) d(\eta)}{\int_{-\infty}^{+\infty} \rho_w^{(2)}(\eta) d(\eta)} \right]^{1/2} = \frac{1}{\mu_{21}} \sigma_y^{(2)} \tag{4.20}$$

Thus Eq. (4.17a) can be rewritten as,

$$<\rho_w^{(1)}> = \frac{\frac{1}{\mu_{21}} \int_{-\infty}^{+\infty} \rho_w^{(2)}(\mu_{21}y) d(\mu_{21}y)}{6 \left(\frac{1}{\mu_{21}} \sigma_y^{(2)} \right)} = \frac{\int_{-\infty}^{+\infty} \rho_w^{(2)}(\eta) d\eta}{6 \sigma_y^{(2)}} \tag{4.21}$$

or,

$$<\rho_w^{(1)}> = <\rho_w^{(2)}> \tag{4.22}$$

That is, the average of damage densities along the trailing edges remains constant during CL propagation. This is the result of the affine transformation of damage evolution. The experimental results shown in *Figure 3.20* support this conclusion.

Similarly, an average density within a process zone $<\rho_A>$, can be proved to be constant during slow crack damage evolution.

Taking $\rho_A^{(1)}(x,y)$ and $\rho_A^{(2)}(x,y)$ as the damage densities within two process zones at time t_1 and t_2, Eq.(4.15) gives,

$$\rho_A^{(1)}(x, y) = \rho_A^{(2)}(\lambda_{21}x, \mu_{21}y) \tag{4.23}$$

The average of $\rho_A^{(1)}(x,y)$ and $\rho_A^{(2)}(x,y)$ can be written as

$$<\rho_A^{(1)}> = \frac{\int_{-\infty}^{+\infty} \int_{-\infty}^{+\infty} \rho_A^{(1)}(x, y) dx dy}{A^{(1)}} \tag{4.24a}$$

$$<\rho_A^{(2)}> = \frac{\int_{-\infty}^{+\infty} \int_{-\infty}^{+\infty} \rho_A^{(2)}(x, y) dx dy}{A^{(2)}} \tag{4.24b}$$

where $A^{(i)}$ ($i = 1,2$) is the area of process zone. Since the process zones here appear as half of the ellipses, the length l_a and the width w of an process zone can be used to calculate the area as

$$A^{(i)} = \frac{1}{2} \pi l_a^{(i)} w^{(i)}$$

(4.25)

The experimental data indicates that the covariance of damage distribution in a process zone is zero, i.e.,

$$\text{Cov}(x, y) = E(xy) - E(x)E(y) = 0$$

(4.26)

where $E(X)$ is the mathematical expectation. Thus the damage distribution in a process zone was independent along x and y directions, that is,

$$\rho_A(x, y) = \rho_A(x)\rho_A(y)$$

(4.27)

On the basis of Eq. (4.27), Eqs.(4.24) can be rewritten as,

$$<\rho_A^{(1)}> = \frac{4}{\pi} \frac{\int_{-\infty}^{+\infty} \rho_A^{(1)}(x)dx}{l_a^{(1)}} \frac{\int_{-\infty}^{+\infty} \rho_A^{(1)}(y)dy}{w^{(1)}}$$

(4.28a)

$$<\rho_A^{(2)}> = \frac{4}{\pi} \frac{\int_{-\infty}^{+\infty} \rho_A^{(2)}(x)dx}{l_a^{(2)}} \frac{\int_{-\infty}^{+\infty} \rho_A^{(2)}(y)dy}{w^{(2)}}$$

(4.28b)

since,

$$\mu_{21} w^{(1)} = w^{(2)}$$

(4.29a)

$$\lambda_{21} l_a^{(1)} = l_a^{(2)}$$

(4.29b)

and,

$$\rho_A^{(1)}(x) = \rho_A^{(2)}(\lambda_{21}x)$$

(4.30a)

$$\rho_A^{(1)}(y) = \rho_A^{(2)}(\mu_{21}y)$$

(4.30b)

it is obtained,

$$\langle\rho_A^{(1)}\rangle = \frac{4}{\pi}\ \frac{\dfrac{1}{\lambda_{21}}\displaystyle\int_{-\infty}^{+\infty}\rho_A^{(2)}(\lambda_{21}x)d(\lambda_{21}x)}{\dfrac{1}{\lambda_{21}}l_a^{(2)}}\ \frac{\dfrac{1}{\mu_{21}}\displaystyle\int_{-\infty}^{+\infty}\rho_A^{(2)}(\mu_{21}y)d(\mu_{21}y)}{\dfrac{1}{\mu_{21}}w^{(2)}} \qquad (4.31)$$

Substituting $\lambda_{21}x = \xi$, $\mu_{21}y = \eta$,

$$\langle\rho_A^{(1)}\rangle = \frac{4}{\pi}\ \frac{\displaystyle\int_{-\infty}^{+\infty}\rho_A^{(2)}(\xi)d\xi}{l_a^{(2)}}\ \frac{\displaystyle\int_{-\infty}^{+\infty}\rho_A^{(2)}(\eta)d\eta}{w^{(2)}} \qquad (4.32)$$

Thus,

$$\langle\rho_A^{(1)}\rangle = \langle\rho_A^{(2)}\rangle \qquad (4.33)$$

Namely, the average of damage densities within the process zones remained the same during CL propagation. This feature is also supported by the experimental results of these studies (*Figure 3.21*).

TABLE III   INERTIA MOMENTS FOR THE SIX CONFIGURATIONS
OF DAMAGE DISTRIBUTION

Configuration		1	2	3⁻	4	5	6
Crack Length (mm)		2.2	3.6	3.8	4.5	4.8	5.5
Total Craze Number (n)	I_0	2,032	5,154	4,382	6,756	10,140	12,932
Refer mm²	I_{2x}	1.504×10^{-2}	3.763×10^{-2}	3.288×10^{-2}	4.652×10^{-2}	5.985×10^{-2}	8.559×10^{-2}
(1/Io)	I_{2y}	6.242×10^{-4}	1.971×10^{-3}	2.591×10^{-3}	3.498×10^{-3}	4.090×10^{-3}	6.235×10^{-3}
to	I_{xy}	0.0	0.0	0.0	0.0	0.0	0.0
Crack mm⁴	I_{4x}	4.716×10^{-4}	2.809×10^{-3}	2.307×10^{-3}	4.399×10^{-3}	7.470×10^{-3}	1.583×10^{-2}
(1/Io)	I_{4y}	8.841×10^{-7}	8.928×10^{-6}	1.491×10^{-5}	2.650×10^{-5}	3.502×10^{-5}	8.786×10^{-5}
Tip	I_{4xy}	8.634×10^{-6}	6.392×10^{-5}	7.286×10^{-5}	1.448×10^{-4}	2.153×10^{-4}	4.400×10^{-4}
Refer mm²	I_{2x}	4.509×10^{-3}	1.045×10^{-2}	1.004×10^{-2}	1.326×10^{-2}	1.728×10^{-2}	2.550×10^{-2}
(1/Io)	I_{2y}	6.242×10^{-4}	1.971×10^{-3}	2.591×10^{-3}	3.498×10^{-3}	4.090×10^{-3}	6.235×10^{-3}
to	I_{xy}	0.0	0.0	0.0	0.0	0.0	0.0
Gravity mm⁴	I_{4x}	4.224×10^{-5}	2.248×10^{-4}	2.144×10^{-4}	3.660×10^{-4}	6.485×10^{-4}	1.485×10^{-3}
(1/Io)	I_{4y}	8.841×10^{-7}	8.928×10^{-6}	1.491×10^{-5}	2.650×10^{-5}	3.502×10^{-5}	8.786×10^{-5}
Center	I_{4xy}	2.559×10^{-6}	1.732×10^{-5}	2.121×10^{-5}	3.957×10^{-5}	6.072×10^{-5}	1.318×10^{-4}
Gravity Center mm	(x_c, y_c)	(0.103, 0)	(0.165, 0)	(0.151, 0)	(0.182, 0)	(0.206, 0)	(0.245, 0)

TABLE IV   INERTIA MOMENTS FOR TWO CONFIGURATIONS OF A PROCESS ZONE

Configuration		Config. 1	Config. 2	Abs. Err	Rel. Err	$I^{(2)}/I^{(1)}$	
Crack Length (mm)		3.0	3.0	0.0	0.0%	-------	-------
Total Craze Number (n)	I_0	2,270	2,386	116	5.0%	1.051	-------
Refer	mm² I_{2x}	1.221×10^{-2}	1.253×10^{-2}	3.2×10^{-4}	2.6%	1.026	$= \lambda^2$
	(1/Io) I_{2y}	8.632×10^{-4}	9.584×10^{-4}	9.5×10^{-5}	10.5%	1.110	$= \mu^2$
to	I_{xy}	0.0	0.0	0.0	0.0%	-------	-------
Crack	mm⁴ I_{4x}	3.224×10^{-4}	3.360×10^{-4}	1.4×10^{-5}	4.1%	1.042	$= \lambda^4$
	(1/Io) I_{4y}	1.757×10^{-6}	2.130×10^{-6}	3.7×10^{-7}	19.2%	1.212	$= \mu^4$
Tip	I_{4xy}	8.570×10^{-6}	10.17×10^{-6}	1.6×10^{-6}	17.1%	1.187	$= \lambda^2 \mu^2$
Refer	mm² I_{2x}	3.855×10^{-3}	3.905×10^{-3}	5.0×10^{-5}	1.3%	1.013	$= \lambda^2$
	(1/Io) I_{2y}	8.632×10^{-4}	9.854×10^{-4}	9.5×10^{-5}	10.5%	1.110	$= \mu^2$
to	I_{xy}	0.0	0.0	0.0	0.0%	-------	-------
Gravity	mm⁴ I_{4x}	3.128×10^{-5}	3.178×10^{-5}	5.0×10^{-7}	1.6%	1.016	$= \lambda^4$
	(1/Io) I_{4y}	1.757×10^{-6}	2.130×10^{-6}	3.7×10^{-7}	19.2%	1.212	$= \mu^4$
Center	I_{4xy}	2.980×10^{-6}	3.322×10^{-6}	3.4×10^{-7}	10.9%	1.115	$= \lambda^2 \mu^2$
Gravity Center	mm (x_c, y_c)	(0.0914, 0)	(0.0928, 0)	1.4×10^{-3}	1.6%	-------	-------
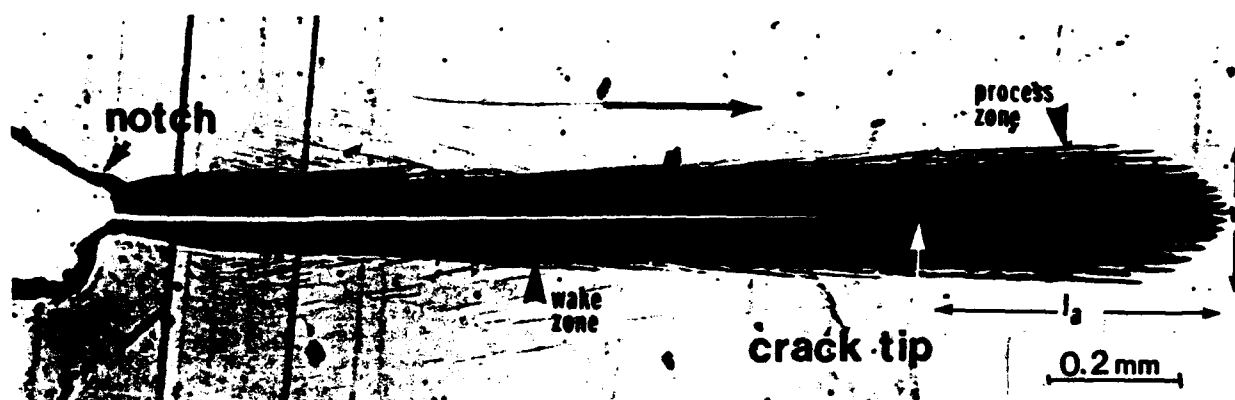
Figure 3.1   Typical configuration of a crack layer in polystyrene
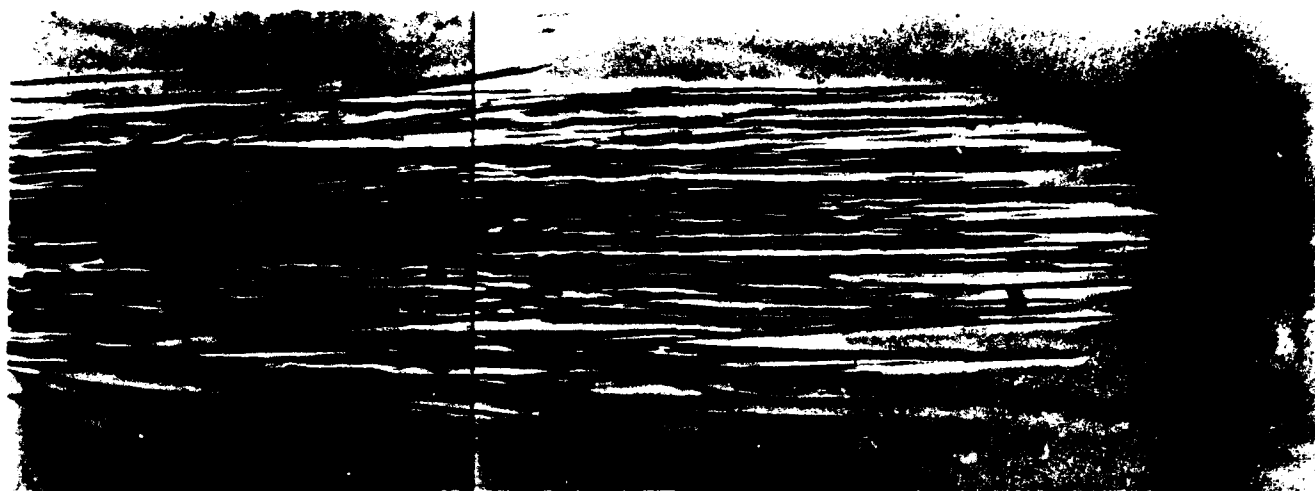
Figure 3.2　　A typical micrograph of polished section of a process zone
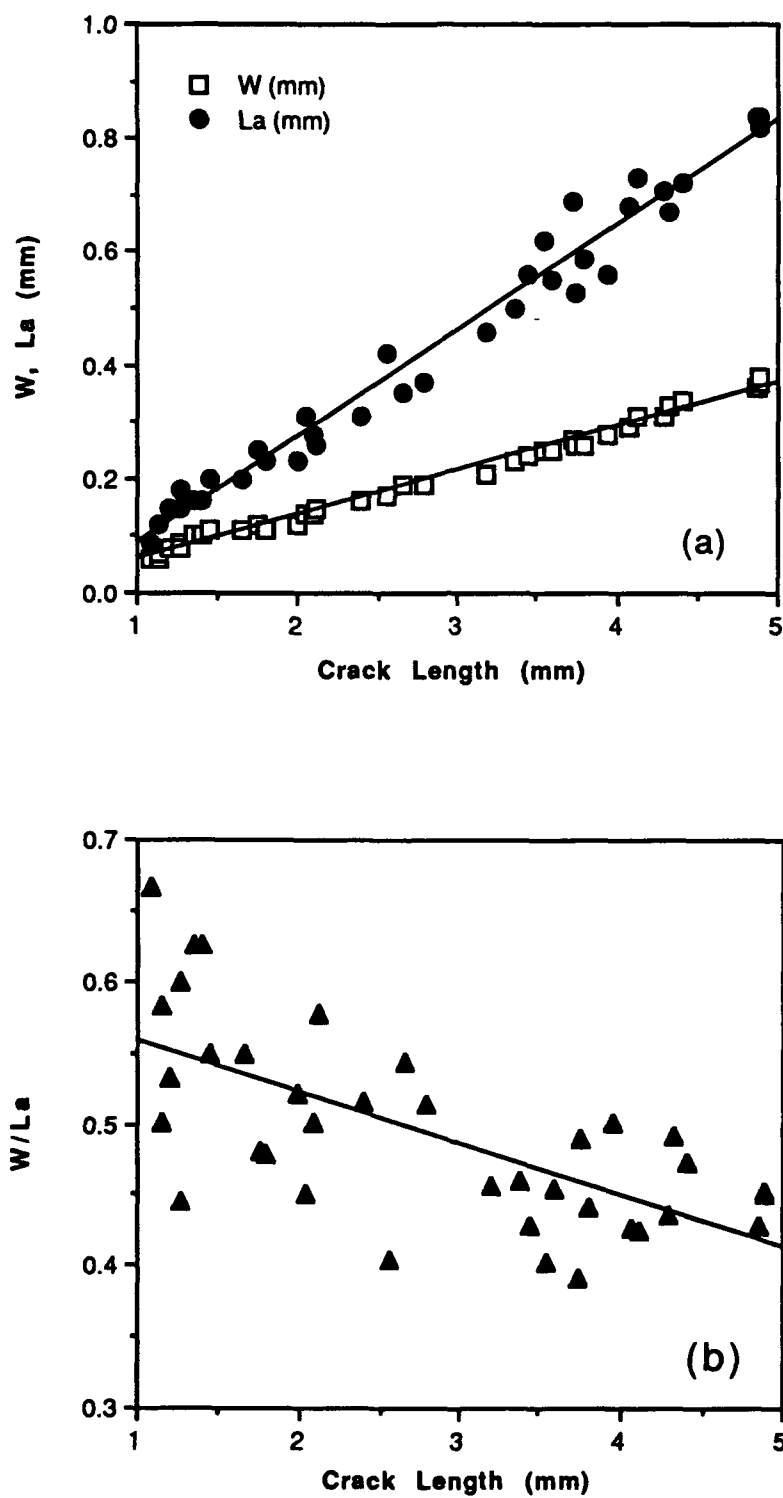
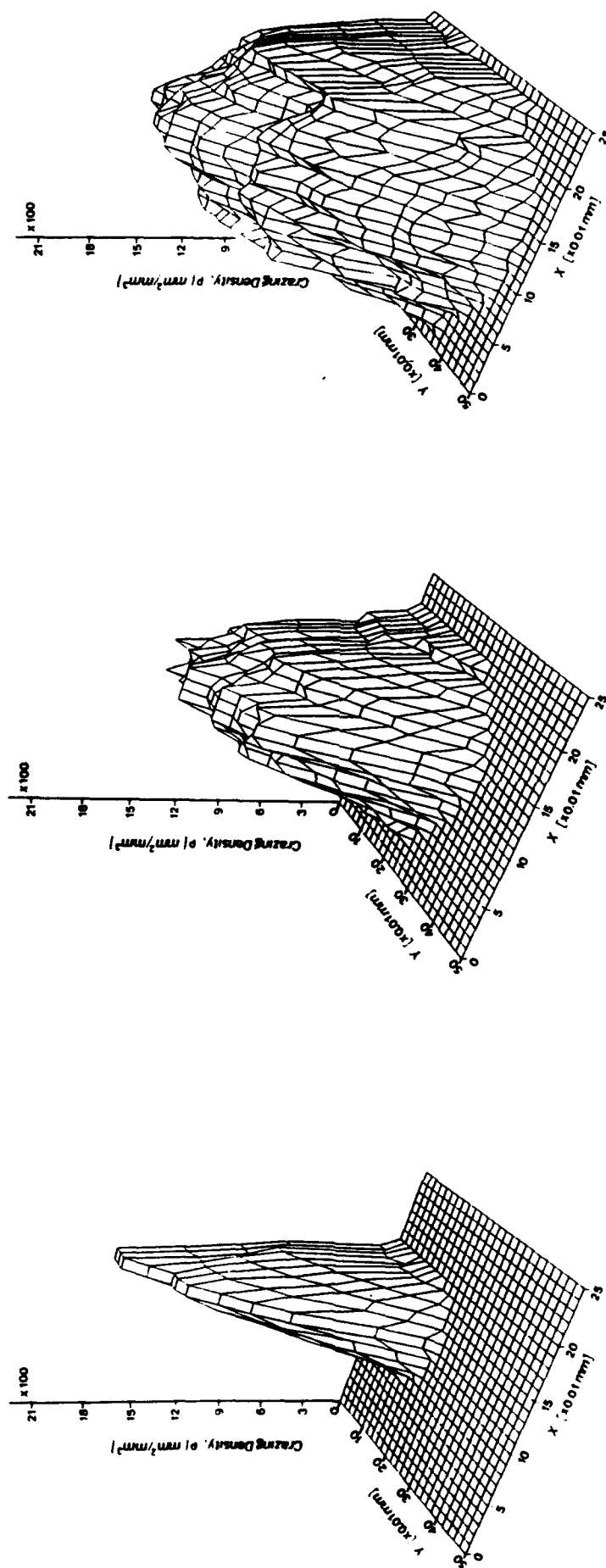***Figure 3.3*** Evolution of (a) w, l_a and (b) w /l_a with crack length

1 mm

Figure 3.4   Configurations of crack and surrounding damage at three
             different crack lengths

Figure 3.5   Three dimensional histograms of damage distribution within the process zones pertaining to the crack layers shown in *Figure 3.4*
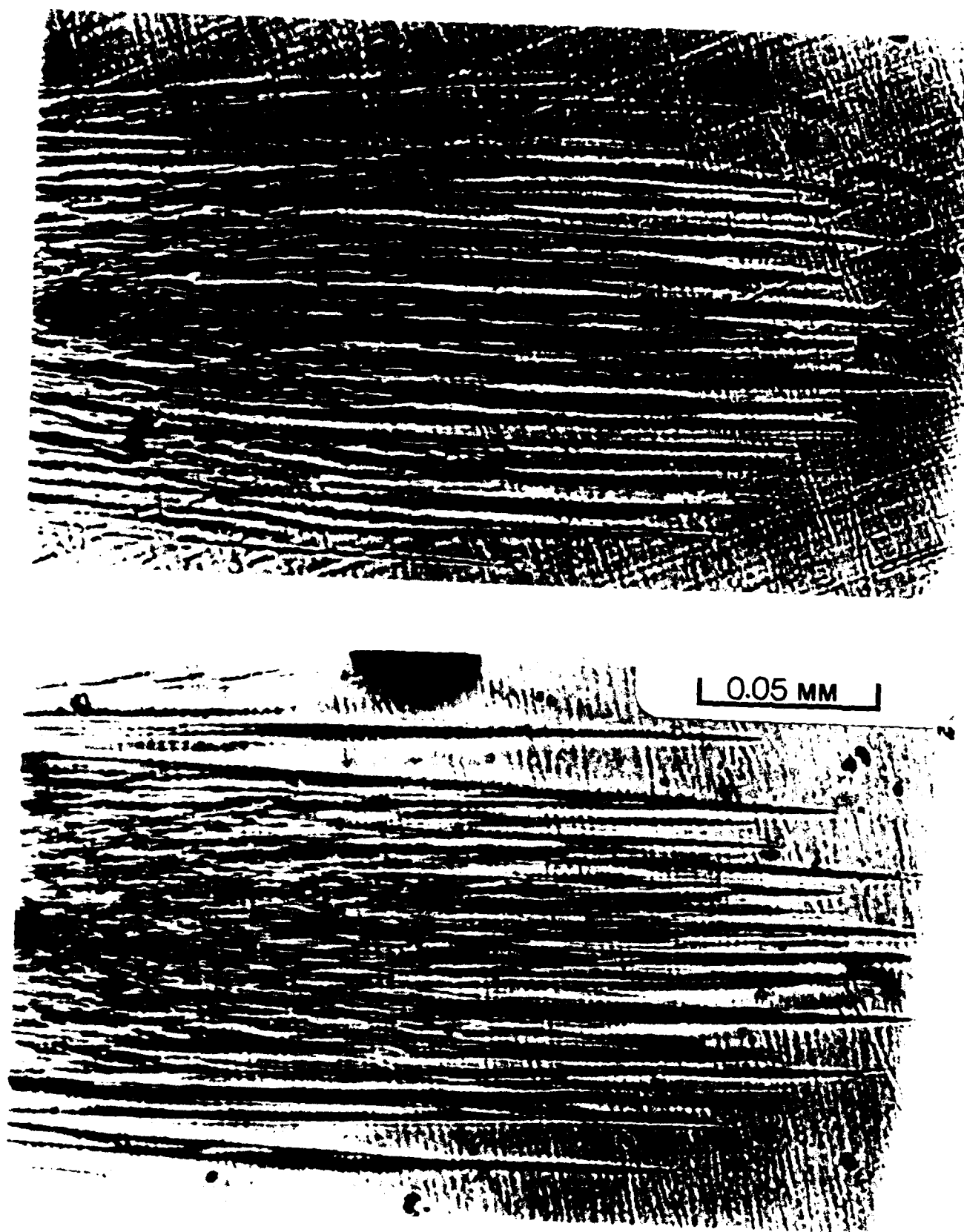
Figure 3.6   Polished sections of two specimens with the same crack length

1500 1200 900 600 300

Specimem-1:

N=41,020 cycles, *l*=3.0mm

*l*a=0.25mm, w=0.14mm

1500 1200 900 600 300

Specimen-2:

N=39,720 cycles. *l*=3.0mm

*l*a=0.25mm, w=0.15mm
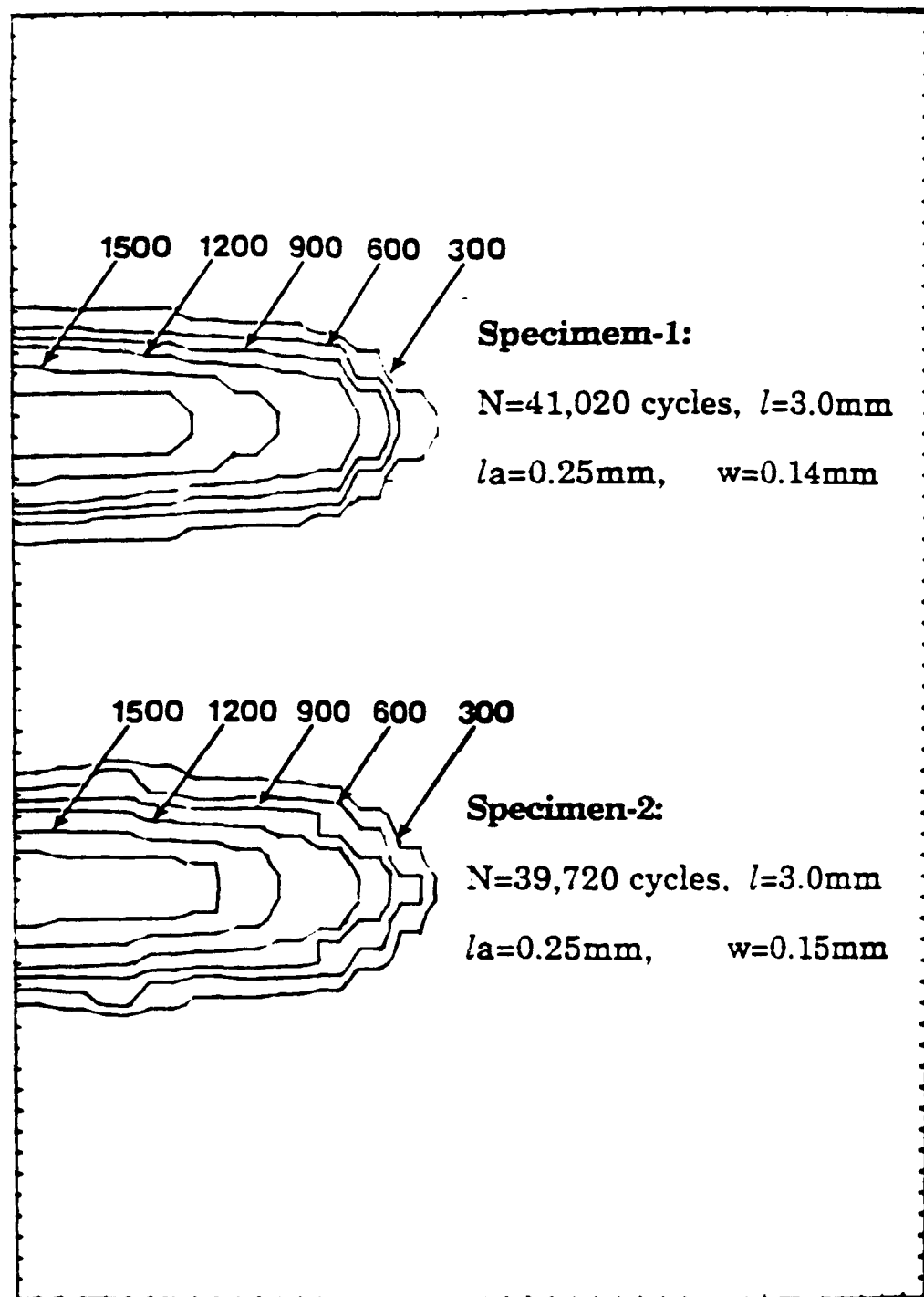
Figure 3.7   Contours of equal damage density within the process zones shown *in Figure 3.6*
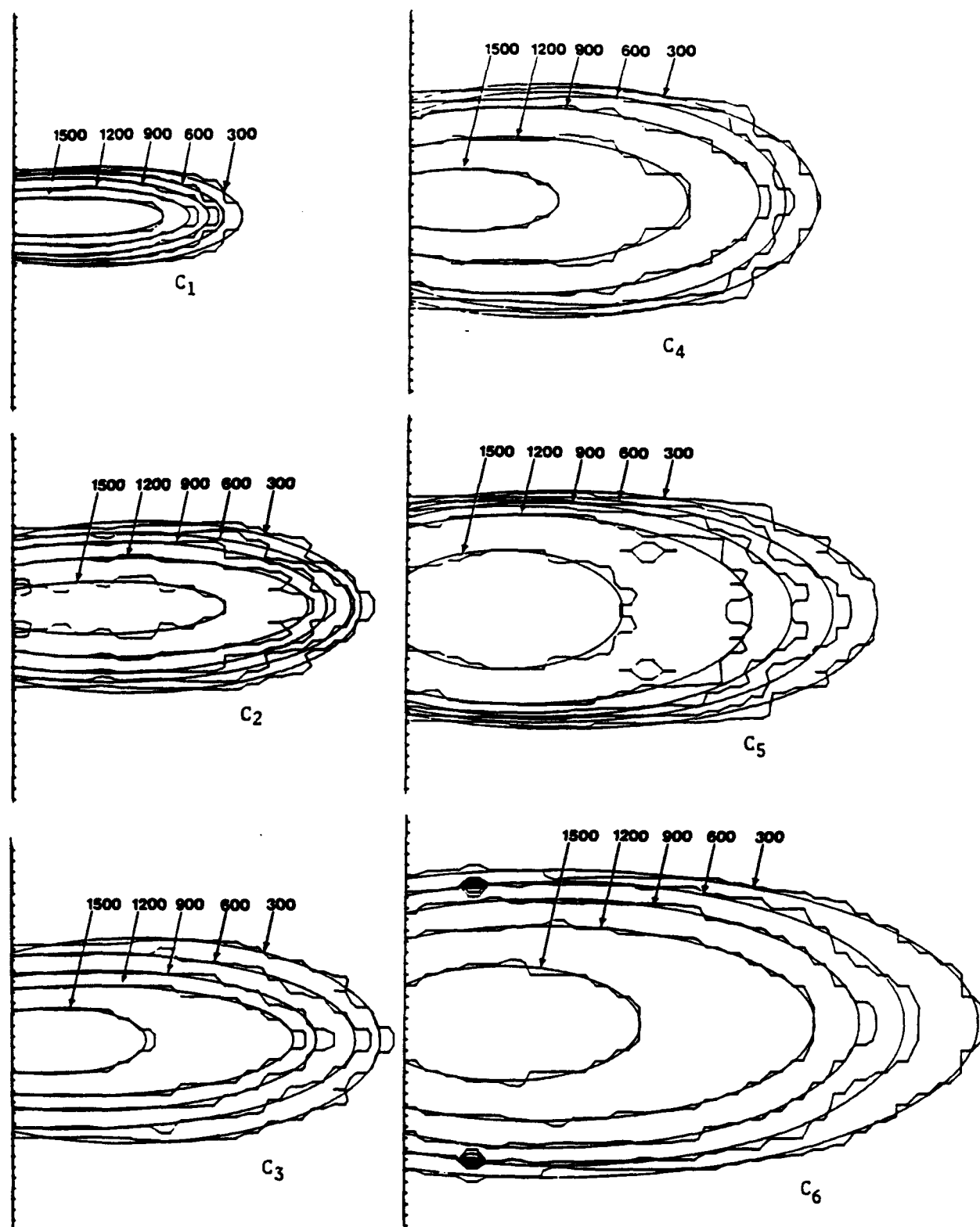
Figure 3.8   Contours of equal damage density within the process zones of six consecutive configurations
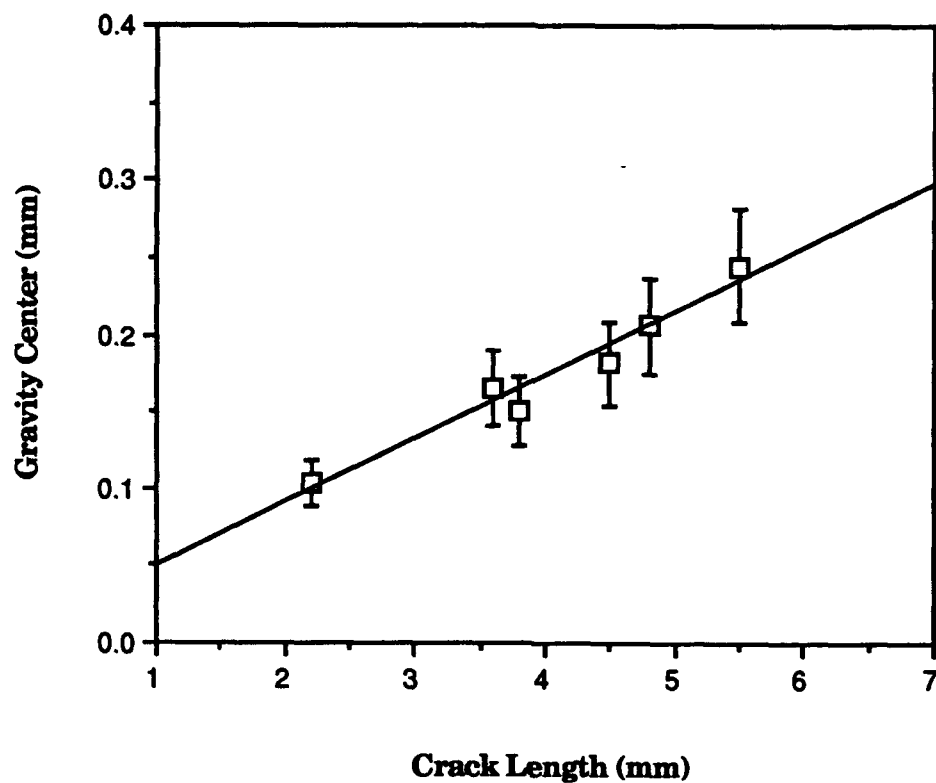
Figure 3.9   The gravity center of process zone as a function
of crack length
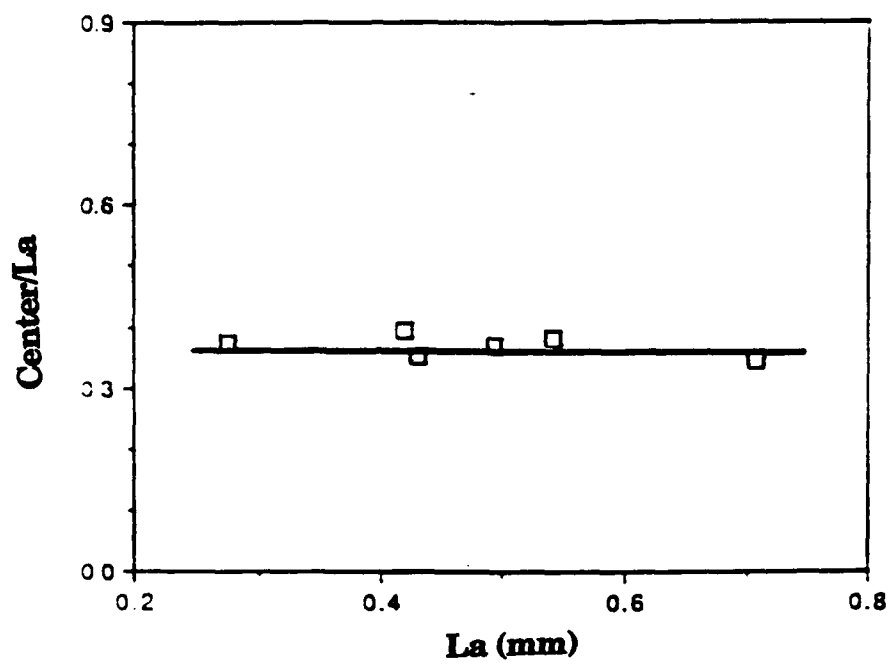
Figure 3.10   The gravity center is located at about 1/3 of La from the crack tip
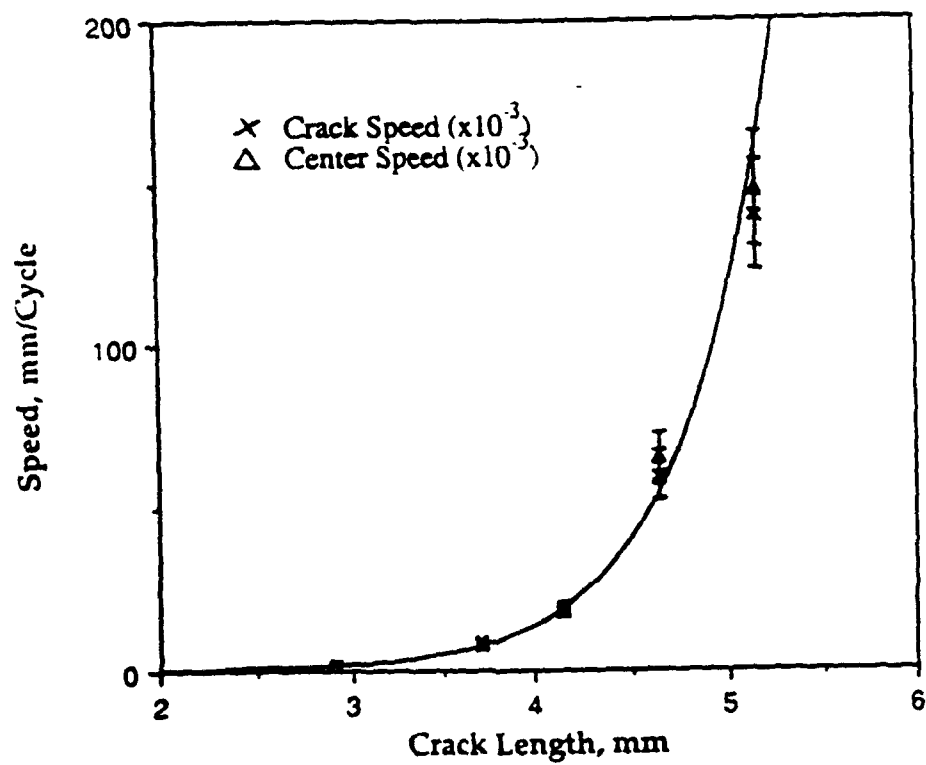
Figure 3.11   The speeds of crack tip and gravity center
as a function of crack length
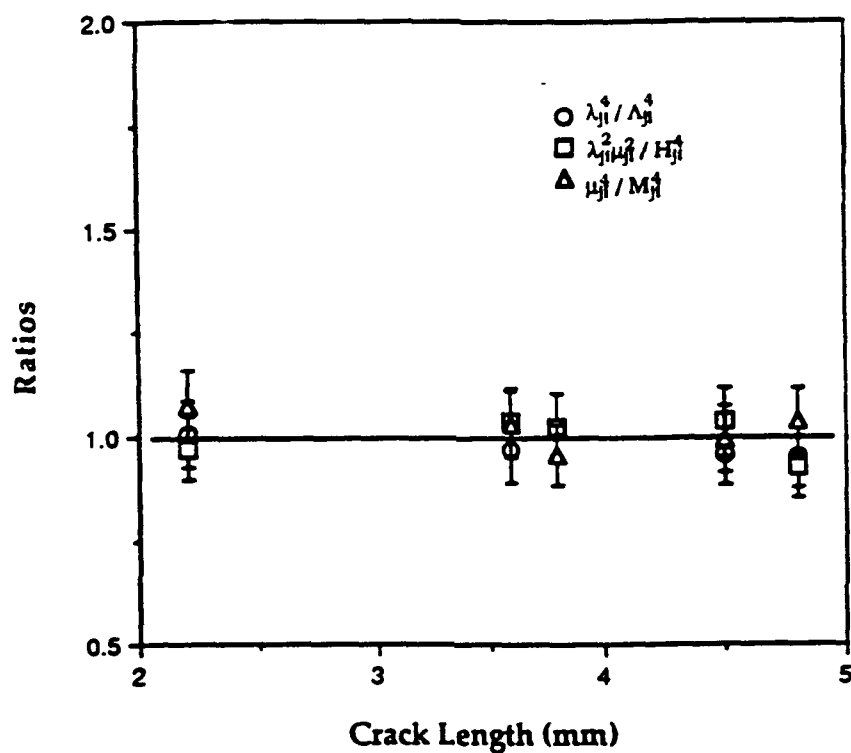
Figure 3.12   Evolution of $\lambda_{ji}^4 / \Lambda_{ji}^4$, μ_{ji}^4 / M_{ji}^4, and $\lambda_{ji}^2 \mu_{ji}^2 / H_{ji}^4$ with crack length
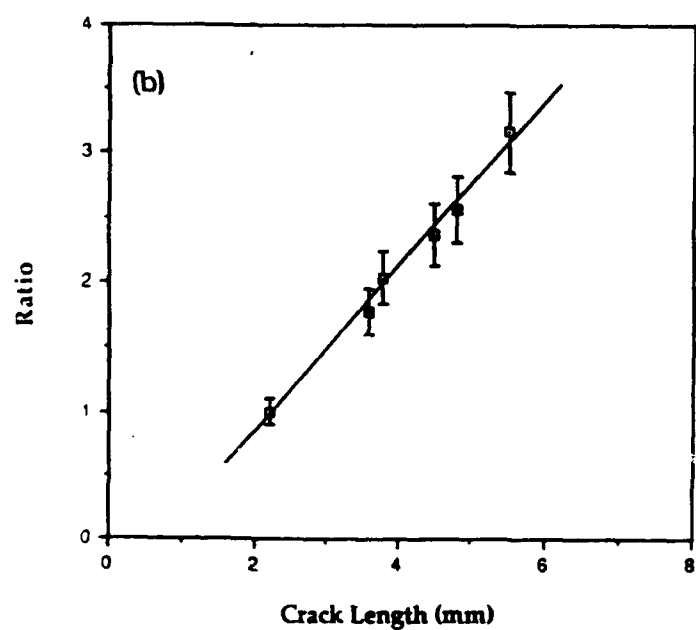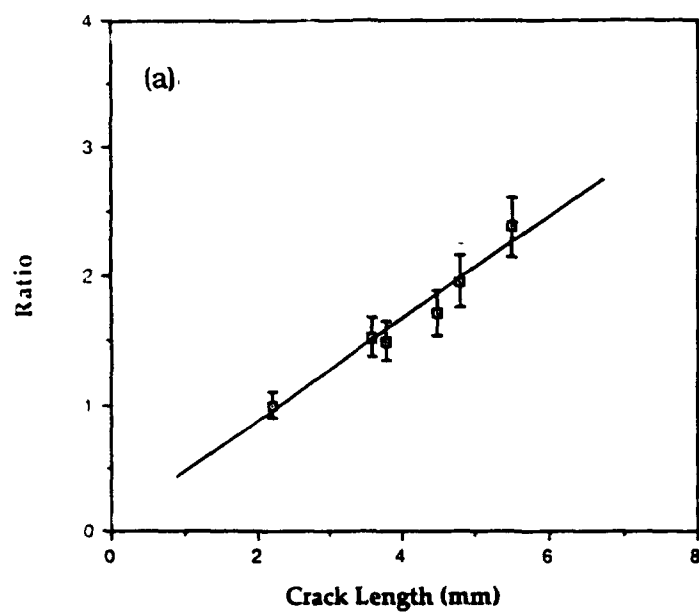
Figure 3.13   Evolution of (a) $\sigma_x^{(j)}/\sigma_x^{(1)}$ and (b) $\sigma_y^{(j)}/\sigma_y^{(1)}$ with crack length
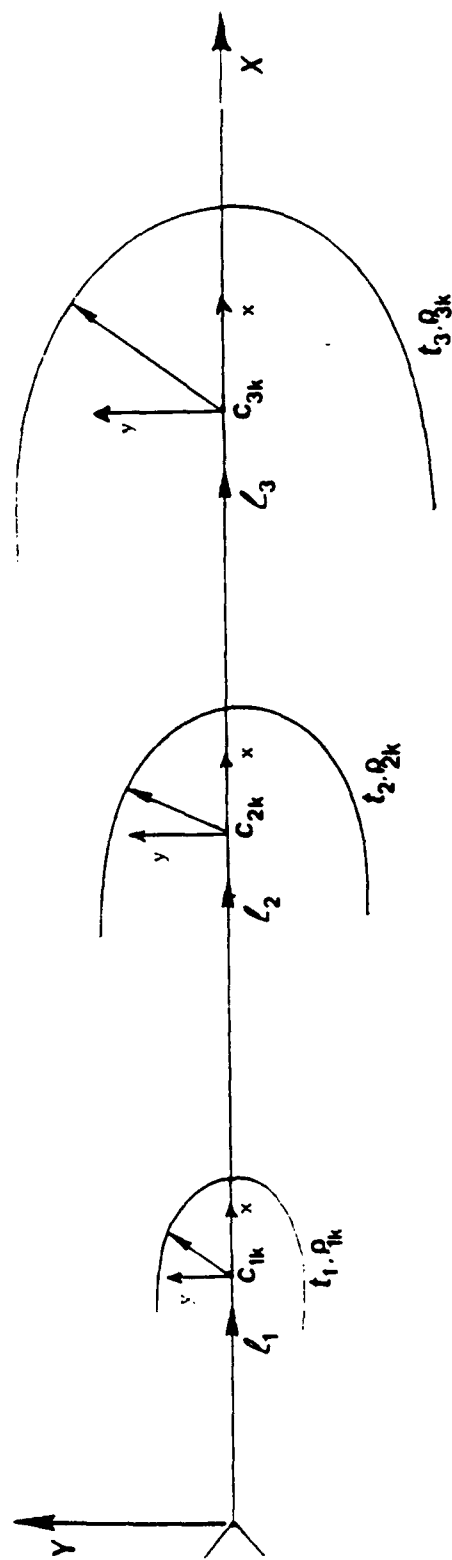
Figure 3.14 Schematic of a contour with equal damage density at consecutive configurations
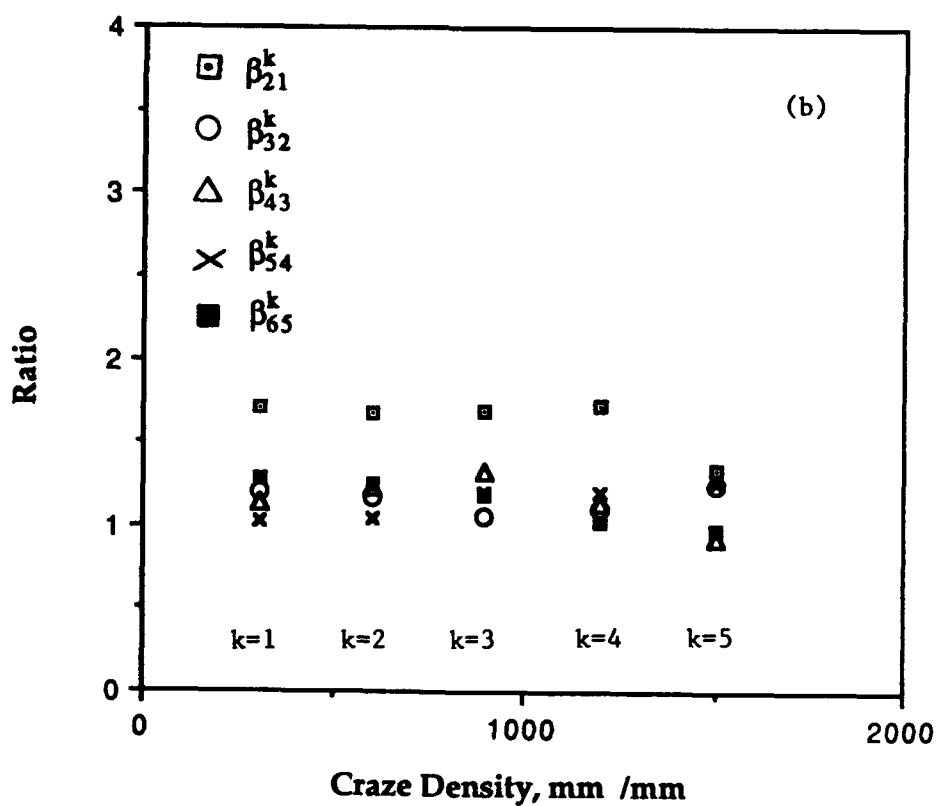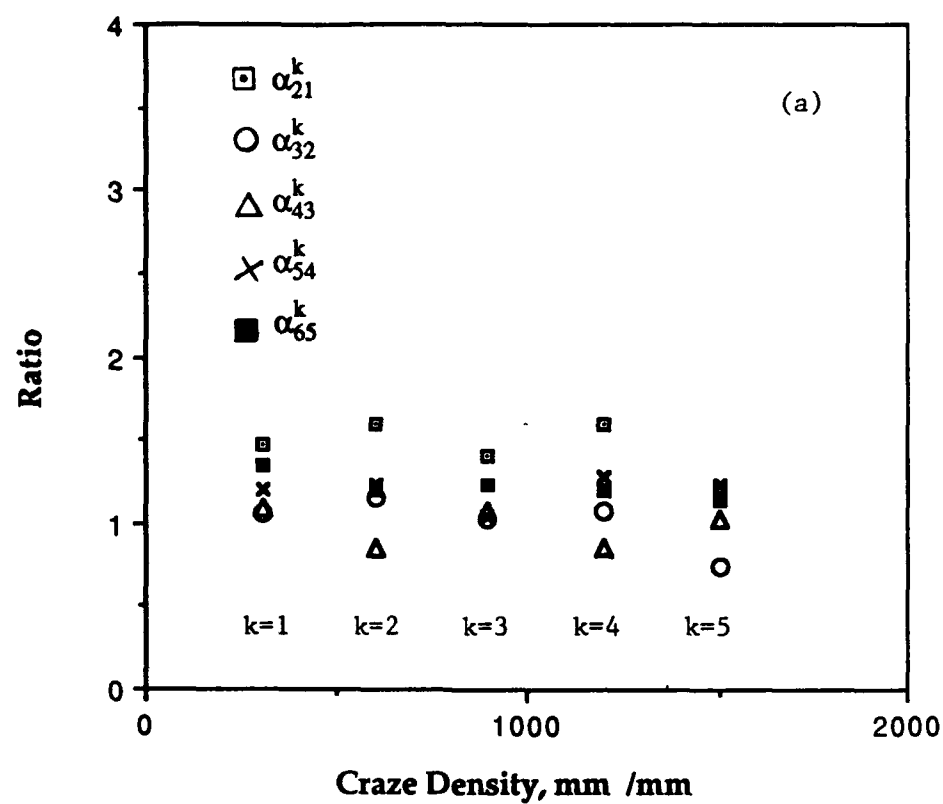
Figure 3.15   Evolution of (a) α_{ji} and (b) β_{ji} with damage density
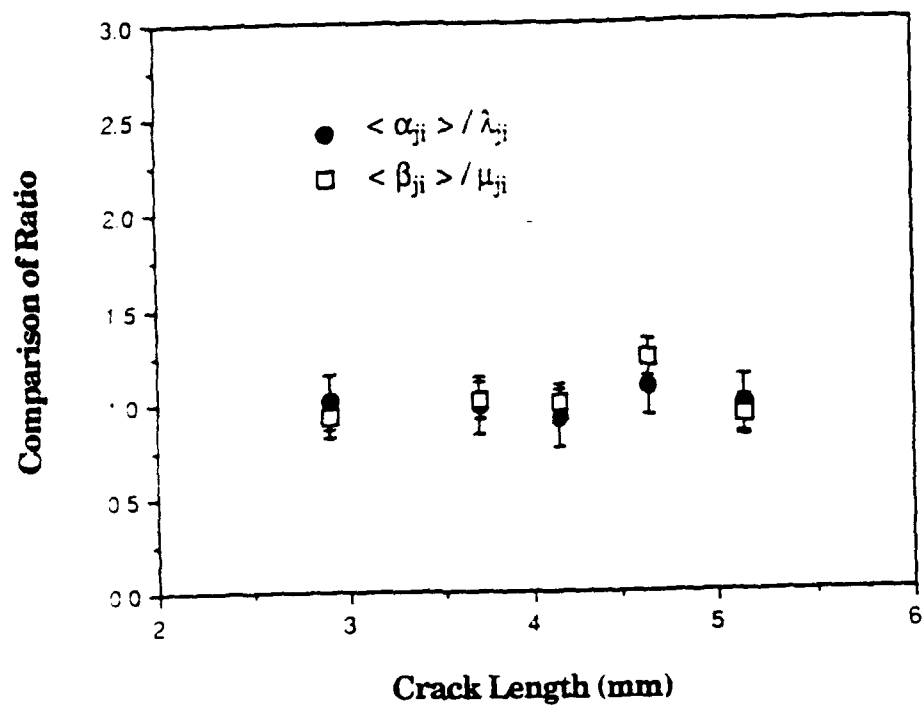
Figure 3.16   Evolution of $< \alpha_{ji} > / \lambda_{ji}$ and $< \beta_{ji} > / \mu_{ji}$ with crack length
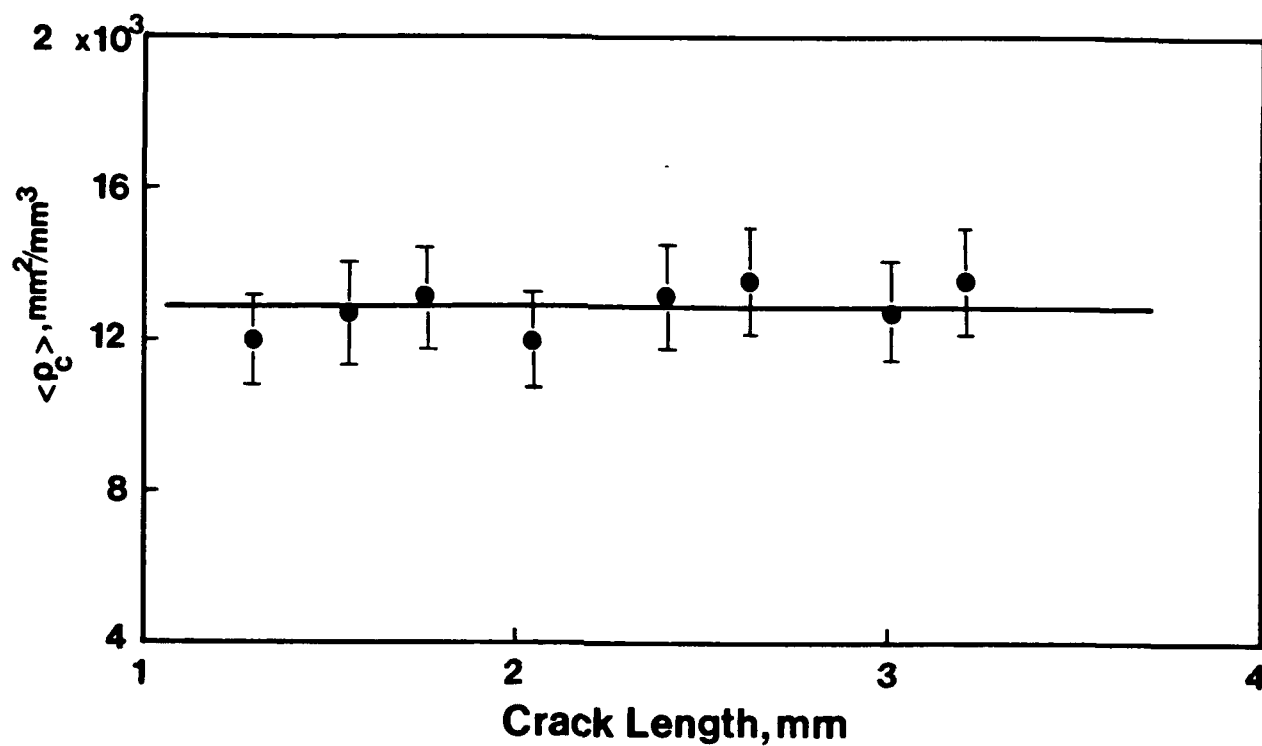
Figure 3.17   Experimental data showing that the damage density within
the core, ρ_c, keeps constant during crack - damage growth
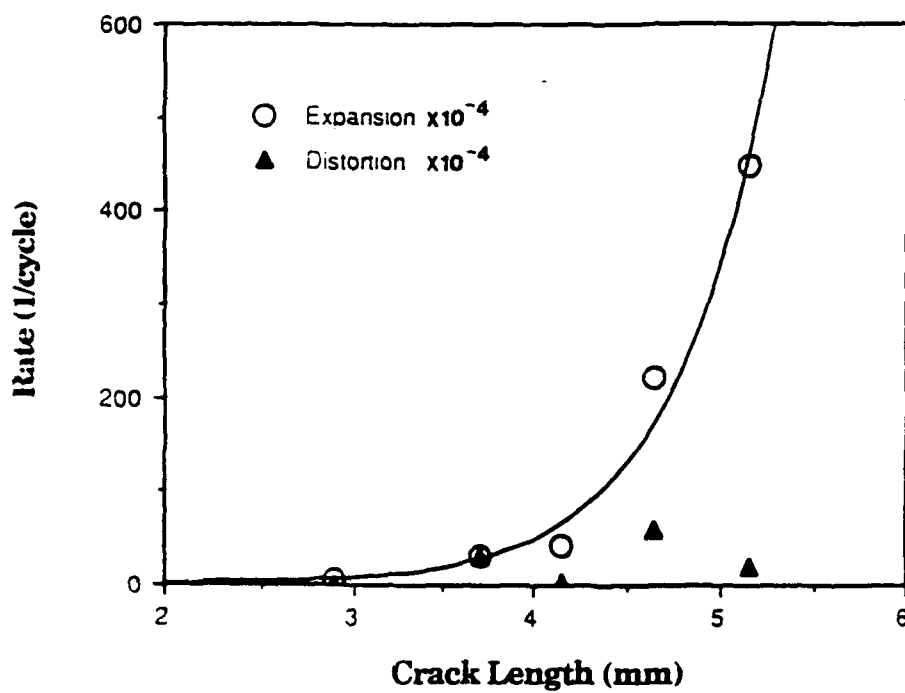
Figure 3.18 The rates of (a) expansion and (b) distortion of the process zone as a functions of crack length

49

Crack Tip

No. Crazes

0   30   60

ρ (mm²/mm³)

0   2400   4800
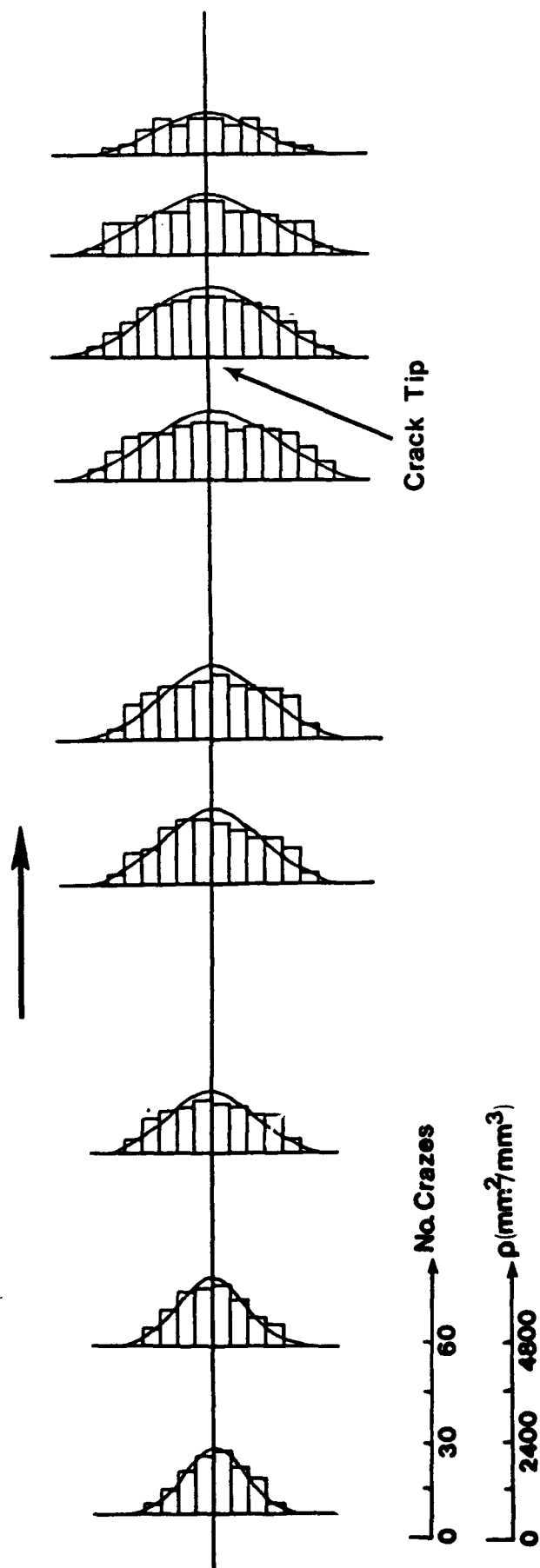
Figure 3.19   Histograms of craze density along the trailing edge
approximated by the function of normal distribution
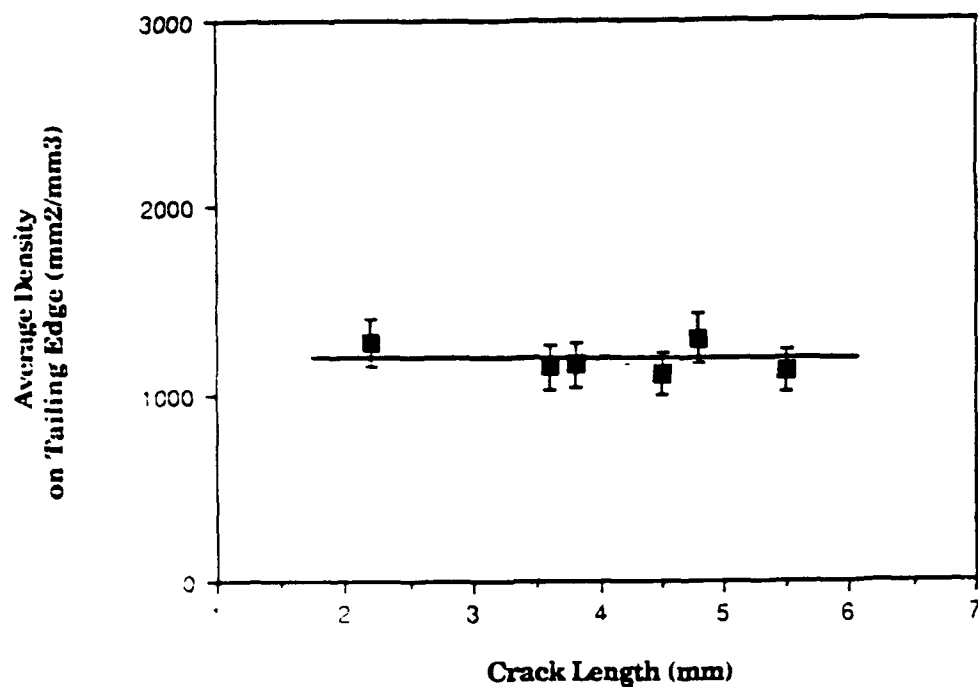
Figure 3.20   Average craze density along the trailing edge as
a function of crack length
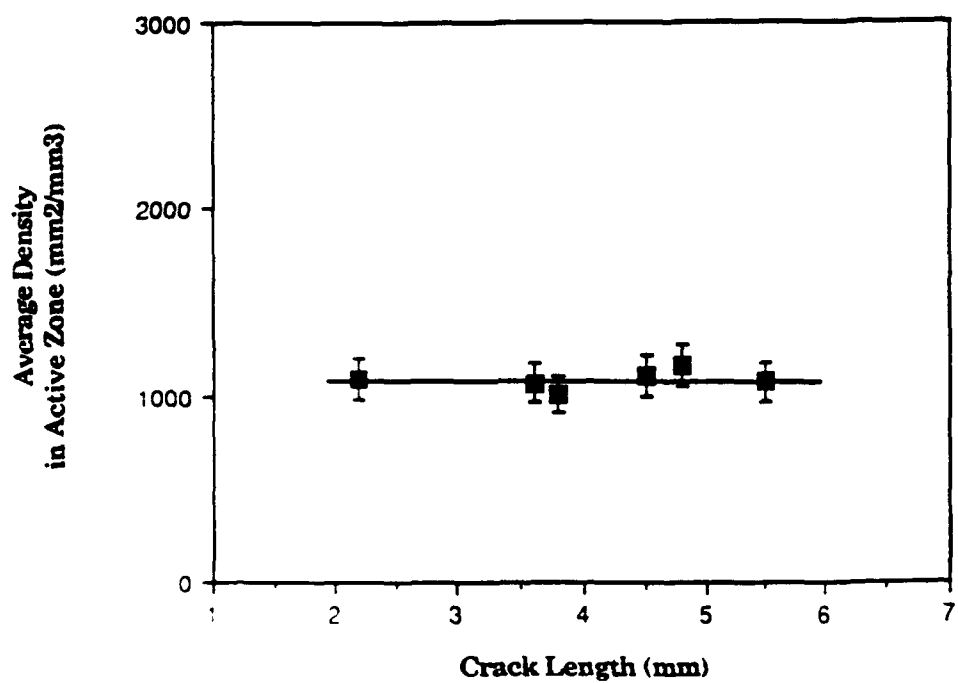
Figure 3.21   Average craze density within the process zone as
a function of crack length

4.EFFECTS OF STRESS RATE AND STRESS LEVEL ON FRACTURE

4.1 Experimental methods

Tension-tension fatigue experiments were conducted on a dual actuator servohydraulic Instron Materials Testing System at ambient temperature in a laboratory atmosphere. All tests were load controlled with a sinusoidal waveform function.

The stress rate and stress level of each experiment were controlled by making appropriate adjustments in the amplitude and the frequency of the loading waveform. Values for the stress rate $\dot{\sigma}$, were calculated from; $\dot{\sigma} = 2 \cdot \nu \cdot (\sigma_{max} - \sigma_{min})$. The geometrical interpretation of this relationship in the stress - time plane is shown in *Figure 4.1*.

In the stress level experiments the stress rate, as defined above, and the minimum stress of the fatigue cycle were held constant (at values of $10.50 \text{MPa} \cdot \text{s}^{-1}$ and 2.50MPa, respectively). The frequency was varied (0.35, 0.75, and 2.00Hz) to achieve maximum stress levels of: 17.50, 9.50 and 5.12MPa, respectively. These values correspond to load ratios, R = 0.14, 0.26, and 0.49.

Similarly, in the stress rate experiments the maximum and minimum stresses were held constant (at values of 7.80 and 2.50MPa) while the frequency was varied (0.33, 1.00, 3.50, 5.00, and 8.00Hz) to achieve stress rates of 3.50, 10.60, 37.10, 53.00 and $84.80 \text{MPa} \cdot \text{s}^{-1}$, respectively. Obviously, in these experiments the load ratio was the same and equal to R=0.32.

The stress intensity factor K_1 was calculated according to the formula:

$$K_1 = \sigma_{max} \cdot \sqrt{\pi l} \cdot f(l/B)$$

Here σ_{max} is the maximum stress of the fatigue cycle, l is the crack length and B is the specimen width. The function $f(l/B)$ is a correction factor related to the specimen geometry [22]. The elastic energy release rate was calculated as $G_1 = K_1^2/E$ where E is the Young's modulus of the material which was evaluated experimentally (E=4.1GPa).

4.2 Results and Discussion

Crack Growth Characteristics

Most of the data on fatigue crack propagation (FCP) reported in the literature are expressed as $\Delta l / \Delta N$, where Δl is the crack length increment that corresponds to the increase in the number of cycles ΔN. Although such a presentation is useful in some cases, the changes in frequency and/or stresses from experiment to experiment makes interpretation of FCP data difficult [23]. To investigate the effects of stress rate and stress level on FCP, we analyze the kinetic data as $\Delta l / \Delta N$ and $\Delta l / \Delta t$ (Note that $\Delta l / \Delta t = \nu \cdot \Delta l / \Delta N$, where ν is the test frequency).

The crack growth kinetics $\Delta l / \Delta N$, for the range of stress rates investigated here, are shown in *Figure 4.2a* as a function of G_1. The data clearly demonstrated that crack speed decreased substantially with the increase in stress rate (or frequency). A similar effect of the test frequency is reported in [24]. On the other hand, if the same data is plotted as $\Delta l / \Delta t$ vs. G_1 (*Figure 4.2b*) the effect of stress rate was relatively small throughout the entire range of slow CL propagation. The largest difference was about half an order of

magnitude and occurs between the largest and smallest stress rates. Similar trend has been observed in polyurethane elastomer [25].

The effect of stress level on FCP is shown in *Figure 4.3*. In both presentations and for small values of G_1, differences in crack speed were relatively small. For relatively larger values of G_1 the differences became greater, the tendency being a faster crack speed with an increase in σ_{max}.

The kinetic data presented in *Figure 4.2b* indicates that the effect of the stress rate was relatively small. If the same data however, is treated as $\Delta l/\Delta N$ vs. G_1 (*Figure 4.2a*), a significant effect of the test frequency was observed. The data showed that the higher the frequency of the fatigue experiment the slower the crack speed. Notice that for a certain crack growth increment Δl, and elapsed time Δt, the corresponding increase in number of cycles is different since $\Delta N = v \cdot \Delta t$. Accordingly, for the same level of G_1 and different values of frequency v, the crack speed $\Delta l/\Delta N$, is smaller when $v>1$, or larger when $v<1$, as compared to $\Delta l/\Delta t$.

For the stress rates (or frequencies) employed in this investigation only negligible temperature rise may take place at the crack tip [26]. Hence the observed crack growth behavior can not be explained in terms of adiabatic heating effects. The influence of the test frequency on FCP has also been attributed to the strain sensitivity of the modulus. For PS however, the modulus is practically insensitive to several decades change in frequency [23]. It is reported in reference [23] that the greatest frequency sensitivity in polymers, which show a high tendency for crazing, would be realized when the frequency of β-transition is comparable to the fatigue test frequency. At room temperature the frequency of β-transition for PS is 10^{-2}Hz. This value is much smaller than the test frequencies employed in the studies reported here.

The effect of frequency on FCP in PS has been reported in references [23]. It has been shown that increasing the test frequency serves to decrease crack growth rates. The behavior has been rationalized by the superposition of fatigue and a variable creep components [23].

Crack growth kinetic data reported in the literature is usually presented as $\Delta l/\Delta N$ vs. the level of stress intensity or energy release rate. Such a presentation however, renders the comparison of kinetic data difficult when the frequency is changed from experiment to experiment. This is because two variables may contribute to the overall crack propagation behavior, stress rate (or frequency) and a creep component which results from the different loading time area (LTA) (the latter can be expressed as the area per cycle or per unit time, under the particular waveform in the stress - time plane, *Figure 4.1*).

To obviate this difficulty, some investigators have examined the effect of loading rate on FCP in polymers by conducting experiments at a certain frequency but with different waveforms [23]. Although an effect of load waveform on crack growth rate was observed, the different waveforms give rise to different LTA/cycle, thus making it difficult to isolate the two effects.

The preceding discussion demonstrates that if different frequencies and the same waveform are employed the LTA/cycle and load rate cannot be isolated. On the other hand, in all stress rate experiments the stress amplitude and mean stress level were kept constant (Sec. 4.1). Accordingly, when the kinetic data is treated as $\Delta l/\Delta t$, the following argument applies. The LTA per second is the same in all experiments when Δt is a multiple of the cyclic period T, of the experiment with the smallest frequency ($v=0.33$Hz, $T \approx 3$sec). When Δt is not a multiple of T the differences in LTAsec^{-1}, from experiment to

experiment, are negligibly small when measurements are made over several seconds. This is the case when the average crack speed is low. In the present studies these differences were expectedly small. Differences in LTAsec^{-1} would become relatively large shortly before specimen fracture (last one or two measurements) because the average crack speed is high and measurements may be made at time intervals shorter that T (Note that the magnitude of the differences depends upon the frequencies used). This problem can be avoided if fracture surfaces display clear striations and crack growth occurs with every cycle prior to specimen fracture. Accordingly, the last points of crack propagation could be obtained from fracture surfaces so that Δt is a multiple of T. If this is not the case, evaluation of LTAsec^{-1} for every experiment requires accurate crack growth measurements. However, this is experimentally difficult to obtain with conventional optical techniques. Although, fracture surfaces of the material used in these studies [27] display striations, it was difficult to establish a correspondence between striations and number of cycles. Thus with the exception of the last one to two points, which may not have comparable LTAsec^{-1}, crack propagation behavior shown in *Figure 4.2b* was assumed to be the result from variations in stress rate only.

The data in *Figure 4.2* indicates that while the stress rates, 3.50, 10.60 and 37.10MPa·s^{-1} have a negligible effect on crack growth kinetics, a tendency to higher kinetics was observed for the stress rate of: 53.00 and 84.80MPa·s^{-1}. The largest difference was less than half an order of magnitude and was observed between the smallest and greatest stress rate.

Figure 4.4 displays a transverse section of the lower part of a fractured specimen. Note that crazes are uniformly distributed along the thickness direction, and craze density increases monotonically towards the fracture surface. Thus analysis of craze distribution on sections parallel to the plane of the specimen was sufficient.

Figure 4.5 displays parallel sections of the lower half of specimens fractured under the stress rates, $\dot{\sigma}$ = 3.50, 37.10 and 84.80 MPa.s^{-1} and which correspond to the same level of G_1. Similar sections of the three specimens fatigued under the three stress level are shown in *Figure 4.6*. Interestingly, crazing decreases with the increase in stress rate and increases with the increase in stress level.

The micrographs of *Figure 4.5* show that the smaller the stress rate the larger the amount of crazing around the crack path. Therefore one would expect higher kinetics with the increase in the stress rate since more energy is spent on damage formation and growth, and less on crack propagation. Although this this seems to be the case for $\dot{\sigma}$=53.00 and 84.80MPa·s^{-1}, the differences in kinetics observed under the stress rates of: 3.50, 10.60 and 37.10MPa·s^{-1} were negligible. This may be due to the fact that craze nucleation and growth are relatively low energy processes. Consequently, it was difficult to record changes in the total potential energy of the specimen caused by craze nucleation and growth through mechanical experiments. Therefore, inspite of the different amounts of damage observed, its effect on crack speed was not seen.

In the different stress level experiments we changed the levels of σ_{max} while keeping $\dot{\sigma}$ and σ_{min} of the fatigue cycle the same. These experimental conditions were achieved by employing different frequencies at each experiment (Sec. 4.1). That is, we could not investigate the effect of load level having the same load rate without changing the frequency. The range of frequencies employed in the load level experiments however, have a negligible effect on crack propagation when data was treated as $\Delta l / \Delta t$ (*Figure 4.2*). Accordingly, it is assumed that the effect of test frequency and any possible cross effects resulting from changes of σ_{max} and frequency were negligible in the data shown in *Figure 4.3*.

The kinetics of crack growth for the different stress level and same stress rate experiments are plotted in *Figure 4.3* as $\Delta l / \Delta t$ vs. G_1. Here, the change in σ_{max} results in different LTA/s from experiment to experiment, the tendency being larger LTA/s with the increase in σ_{max}. Furthermore, it was not possible to isolate the effect of stress level and LTA/s when the stress rate was kept constant. Hence the behavior of crack growth (*Figure 4.3*) may be due to both stress level and LTA/s. Note that the same arguments apply when the data was treated as $\Delta l / \Delta N$ vs. G_1.

The micrographs of *Figure 4.6* indicate that the greater the stress level the larger the extent of crazing around the crack path. If the energy spent for damage controls crack growth, larger damage zones would result in lower FCP. The crack growth kinetics however, shows an opposite trend (*Figure 4.6*).

When a crack is surrounded by a zone of crazes, the energy release rate G_1, is distributed between the crack itself and the damage. The relative distribution depends upon the specific energy for craze formation, amount of crazing and its effect on the crack tip stress. The extent to which crack - craze interaction and amount of crazing contribute to fracture behavior of the material reported herein is a function of craze distribution, their length and opening at various stages of their development. It was difficult however, to assess their contribution with the available experimental and analytical techniques. Answers to these questions should await for more refined analytical methods and improved experimental techniques to be developed.

Damage Evolution Characteristics

From micrographs similar to one displayed in *Figure 4.5* and *4.6* we construct histograms of craze density $\rho(mm^2/mm^3)$ [28], along straight lines normal to the crack growth direction. These histograms were compared by examination of the ratio of the second moment μ_2 to the square root of the fourth moment $\sqrt{\mu_4}$. The evolution of these ratios is shown in *Figure 4.7* as a function of the energy release rate G_1. The data suggests that for each experimental condition, $\mu_2/\sqrt{\mu_4}$ was approximately constant throughout the stable phase of CL propagation. Moreover, it is worth noticing that the ratio was the same for all three stress level experiments.

The data in *Figure 4.7* indicates that for each loading condition the ratios $\mu_2/\sqrt{\mu_4}$ remains constant throughout the slow CL propagation. These findings support the results reported in Chapter 3 of this report. Moreover, it is worth noting that $\mu_2/\sqrt{\mu_4}$ was independent of the stress level (*Figure 4.7*). These results may be looked upon as a similitude criterion for the particular fracture process reported herein.
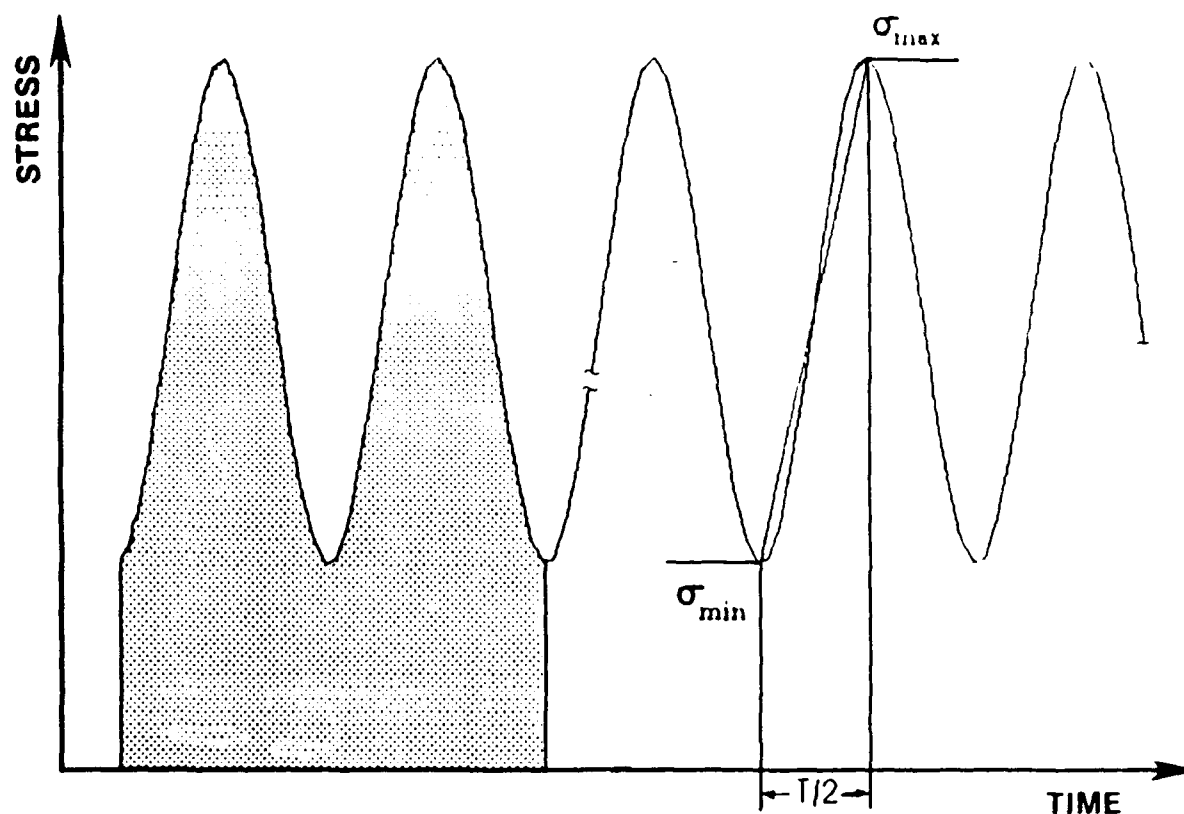
Figure 4.1   Definition of the stress rate.
The shaded area indicates load time area
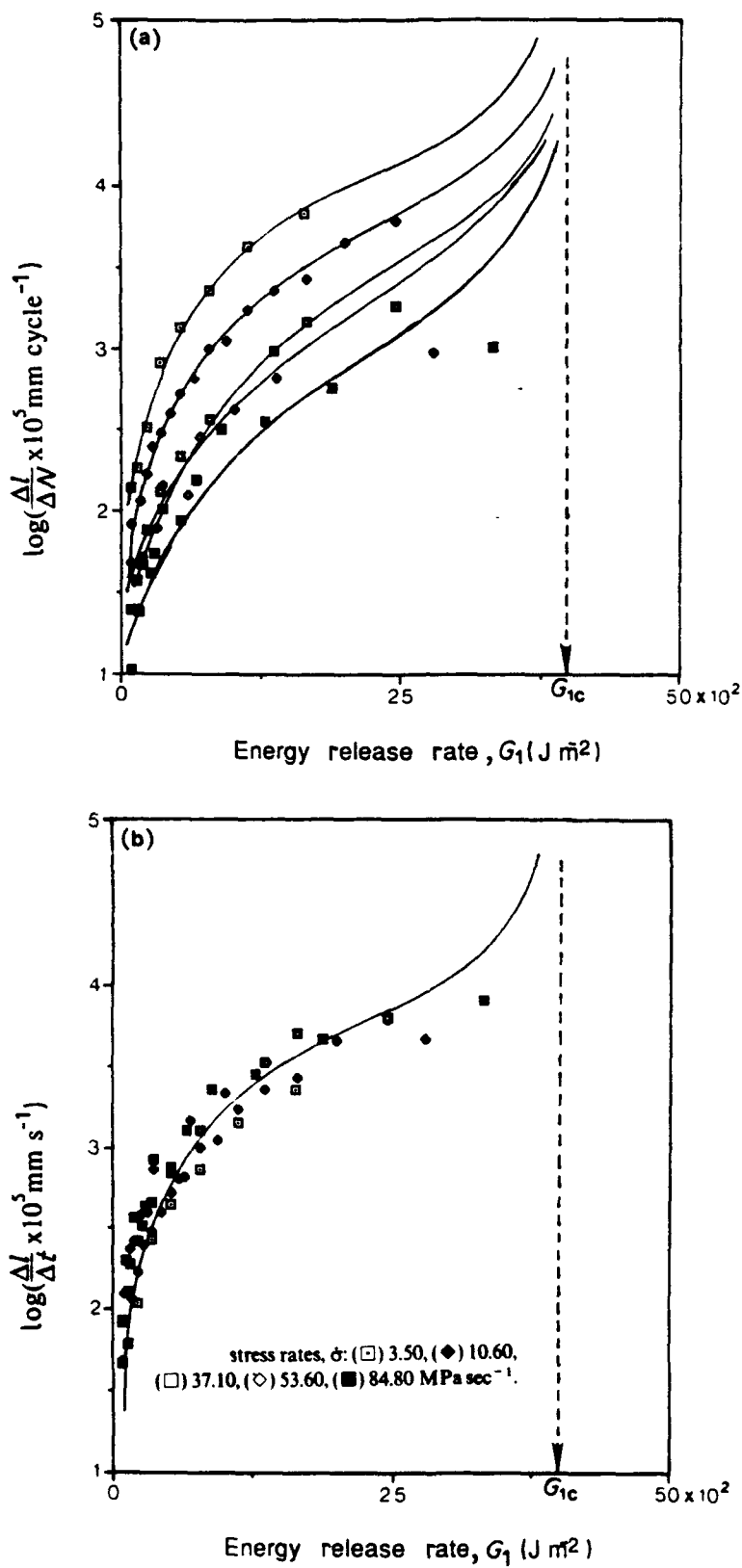
Figure 4.2   Crack growth kinetics: (a) $\Delta l / \Delta N$ and (b) $\Delta l / \Delta t$, plotted against G_1 for five different stress rates
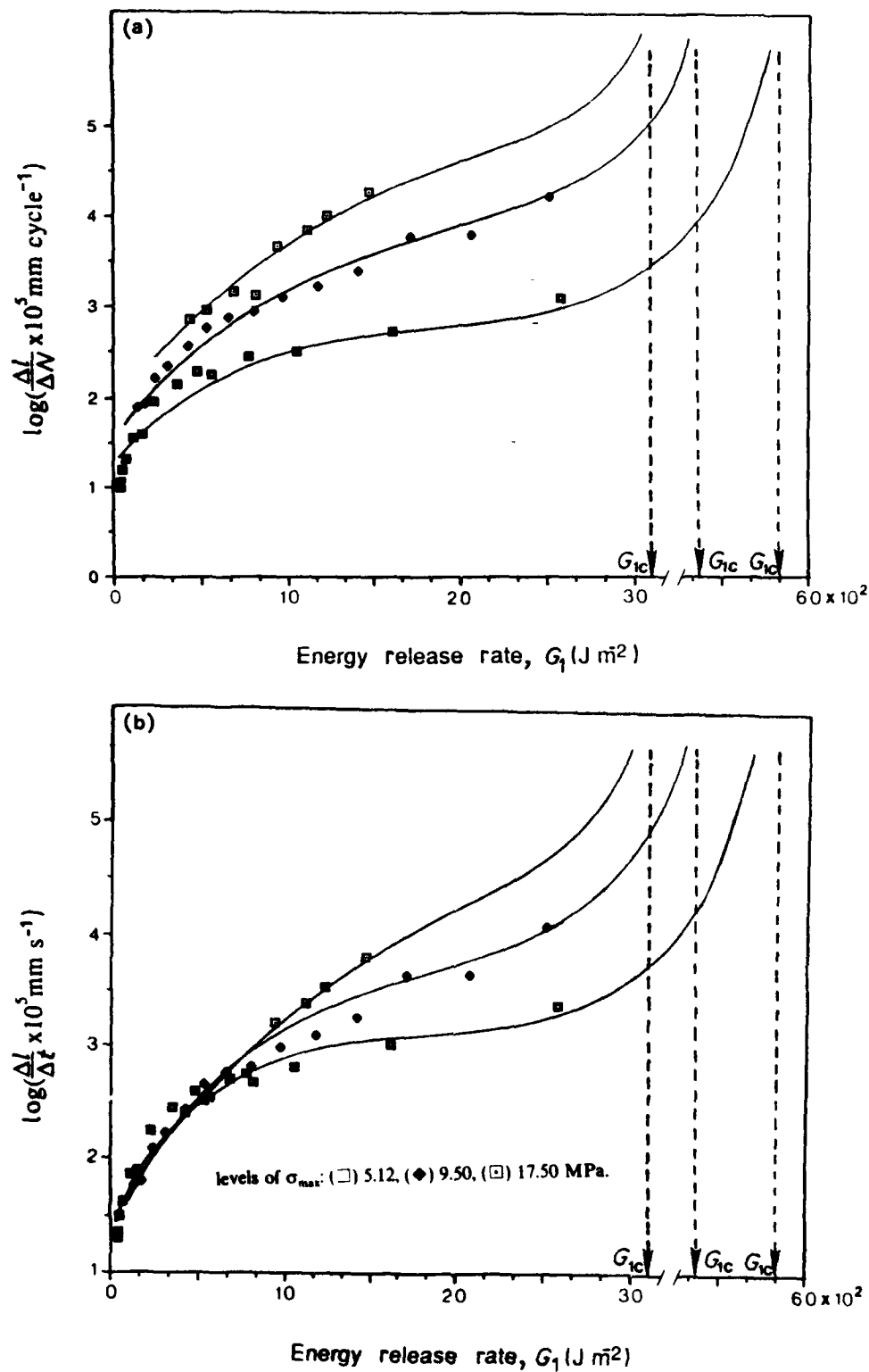
Figure 4.3   Crack growth kinetics: (a) $\Delta l / \Delta N$ and (b) $\Delta l / \Delta t$, plotted against G_1 for three levels of σ_{max}

0.05 mm

Figure 4.4   Transverse section of the lower half of a fractured specimen which corresponds to the slow CL propagation
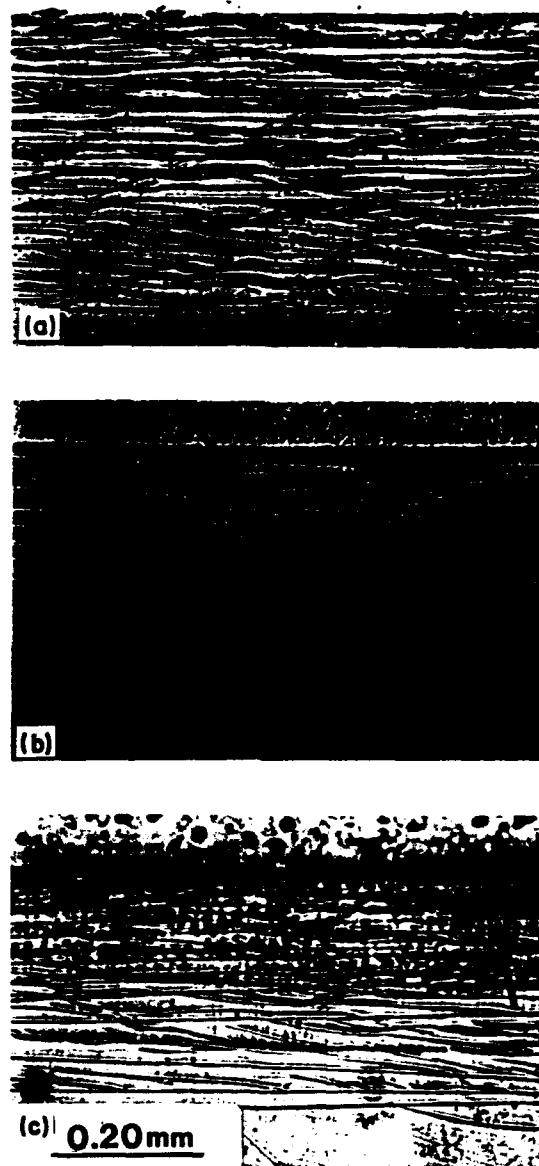
Figure 4.5   Lower parts of parallel sections of specimens fractured under
three different stress rates and which correspond to $G_1=15 \times 10^2 J/m^2$
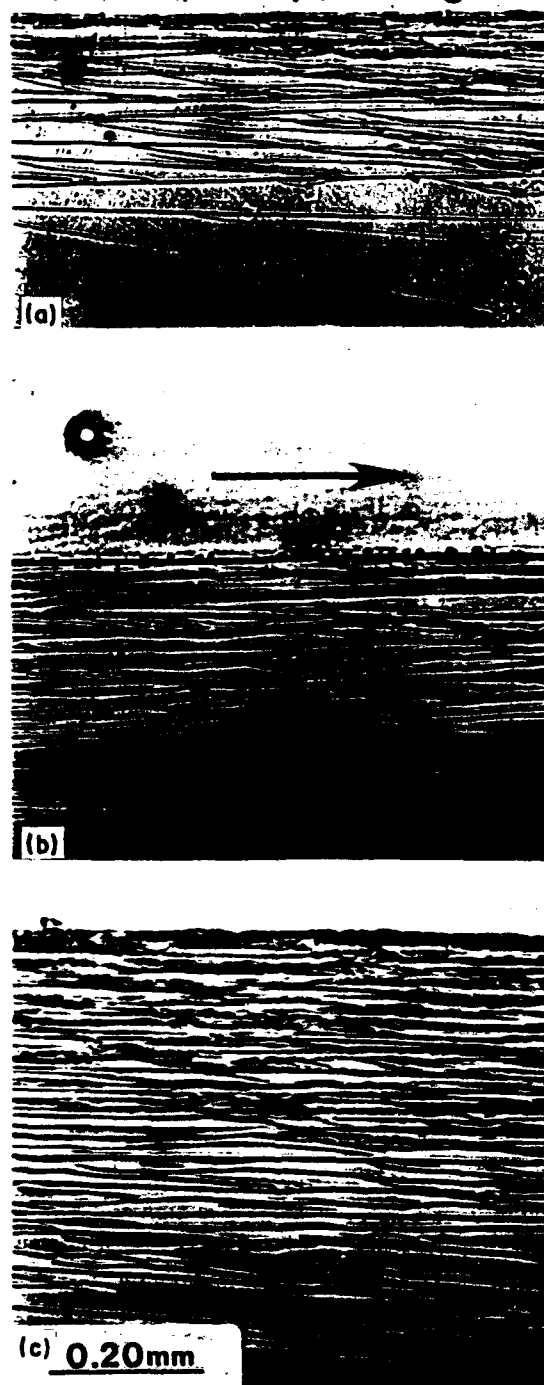
Figure 4.6   Lower parts of parallel sections of specimens fractured under three different stress levels and which correspond to $G_1=15x10^2J/m^2$
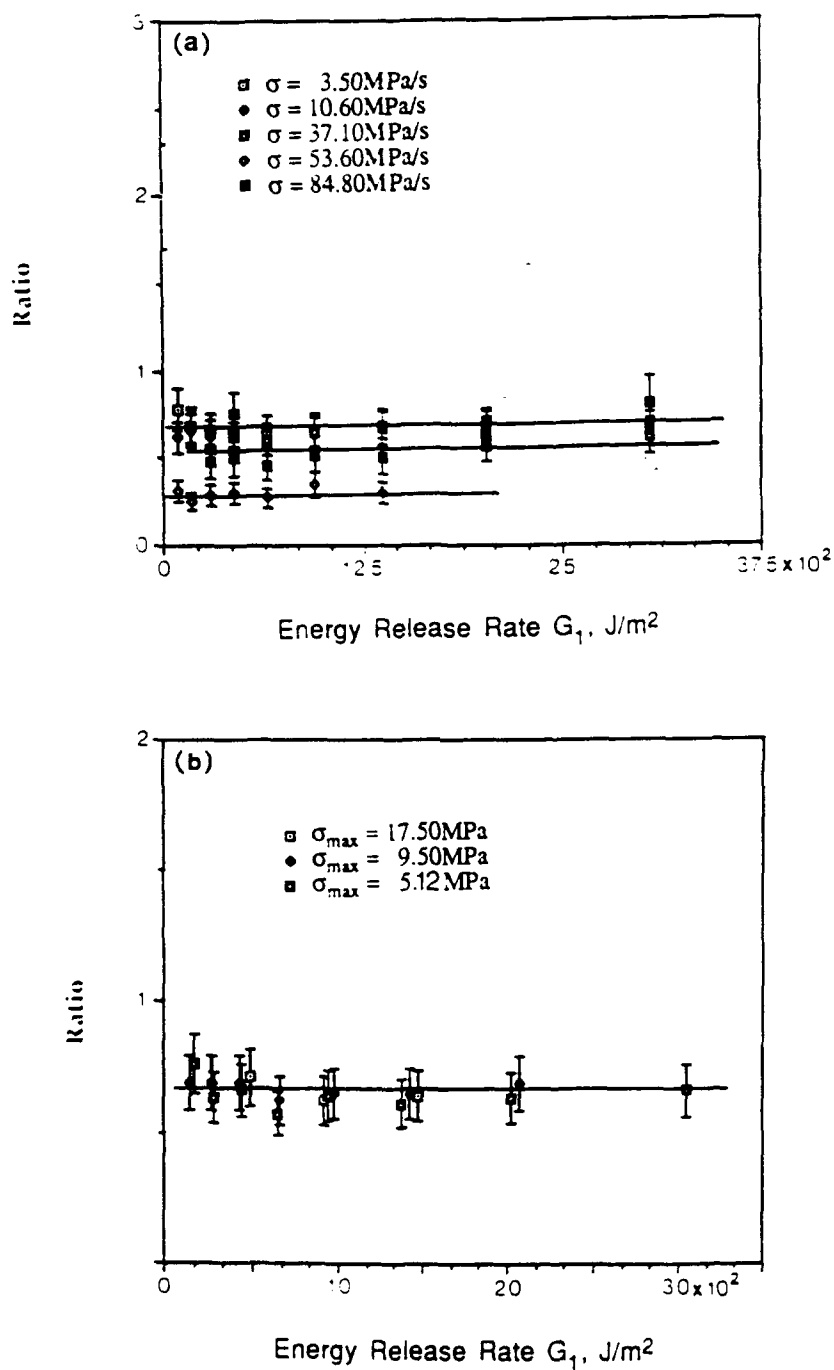
Figure 4.7   Evolution of ratios $\mu_2/\sqrt{\mu_4}$: (a) for the different stress rates, (b) for the different stress levels

5. CONCLUSIONS

Crack Initiation

1. Experimental investigations on crack initiation on a model material reveal two damage patterns: a core of highly localized damage and peripheral less dense damage.

2. Damage evolution before crack initiation can be described by a linear function of the space variables. In addition, the damage zone evolves by the translation and self - similar expansion. -

3. The behavior of an average damage density before crack initiation is of a damping character and seemingly approaches a constant value at initiation.

4. Crack initiates within the highly localized core of damage.

5. While the pattern of the peripheral damage is load history dependent, damage density within the core of damage is found independent of the loading conditions. Accordingly, the difference in time to crack initiation due to different loads is attributed to the effects of damage surrounding the core zone.

6. The core zone is found to grow exponentially with the energy release rate.

Crack Propagation

7. Damage evolution within a process zone can be approximated by a linear approximation of the space variables. The fracture process can be described by the translation and self - similar expansion of the process zone. The distortion of the process zone is found insignificant. Accordingly, the corresponding energy release rates are given by the J_1 and M integrals. The results of the present studies are in agreement with the kinematic assumption of damage evolution described in [19,21].

8. The density of damage in the close vicinity of the crack tip is kept constant during the phase of slow crack growth. This result suggests that a certain level o damage should be reached before crack growth.

9. Damage density at crack initiation is approximately equal to the density of damage in the close vicinity of crack tip.

10. The average damage densities along the trailing edge of the process zone and within the process zone are kept constant during slow crack damage evolution. This is the result of the linear transformation of damage evolution.

11. *The results of these studies indicates the following similarities between the processes of crack initiation and that of crack growth:*
    (a). In both cases damage evolution can be approximated by a linear function of the space variable.
    (b). Crack initiation occurs when damage density reaches a certain level. This same level of damage is kept constant during crack damage evolution. This result suggests that damage density at the location of fracture should reach a certain level before crack initiation and subsequent growth.

12. The effect of stress rate on crack propagation and damage evolution are investigated by conducting experiments with certain frequencies and with constant stress amplitude and mean stress level. *These experimental conditions allow for the isolation of rate and creep contribution if the kinetic data is treated as $\Delta l / \Delta t$ vs the energy release rate G_1.*

The experimental results have shown that:

13. A relatively small effect of the stress rate on FCP is observed when kinetic data is treated as $\Delta l / \Delta t$ vs. G_1 (Fig. 5). When we account for the different frequencies employed in each experiment (i. e., plotting the data as $\Delta l / \Delta N$ vs. G_1) a decrease in crack growth kinetics is seen with an increase in test frequency.

14. An increase in crack growth kinetics results from the increase in stress level.

15. The extent of crazing around the crack path is found to increase with the increase in stress level and decrease with increases in stress rate $\dot{\sigma}$.

16. In both studies damage distributions along directions normal to the crack path are related by a scalar parameter. This scalar parameter is found independent of the stress level. *This result can be looked upon as a similitude parameter for the particular fracture process.*

REFERENCES

1. K. Hellan. in *'Introduction to Fracture Mechanics'*, McGraw-Hill, N.Y. 1984.
2. M. F. Kanninen and C. H. Popelar, in *'Advanced Fracture Mechanics'*, Oxford University Press, N.Y. 1985.
3. R. O. Ritchie, *Int. Met. Reviews*, 5, 1979, p. 205.
4. C. J. Beevers and R. L. Carlson, in *'Fatigue Crack Growth 30 years of Progress'*, R. A. Smith ed., Pergamon Press, N.Y. 1986, p. 89.
5. T. C. Lindley and K. J. Nix, in *'Fatigue Crack Growth 30 years of Progress'*, R. A. Smith ed., Pergamon Press, N.Y. 1986, p. 53.
6. R. O. Ritchie, in *'Advances in Fracture Research, Proc. ICF4'*, S. R. Valluri et.al. eds., Pergamon Press, N.Y. 1984, V. 1, p. 235.
7. D. L. Davidson, and S. Suresh, eds., *Fatigue Crack Growth Threshold Concepts,* The Metallurgical Society of AIME, Pennsylvania 1984.
8. W. A. Wood in *' Treatise on Materials Science and Technology '*, Vol. 5, H. Herman, ed., Academic Press, N.Y. 1974, p. 129.
9. O. Helgeland, *J. Inst. Met.*, 93, 1965, p. 570.
10. M. L. Brown in *Proc. Int. Conf. on dislocation Modeling of Physical Systems*, M.F. Ashby et.al. eds, Pergamon Press, N.Y. 1980, p. 51.
11. H. Murghrabi, in *'Proc. Fifth Int. Conf. on the Strength of Metals and Alloys'*, P. Haasen et.al. Eds, Pergamon Press, N.Y. 1980, Vol. 3, p. 1615.
12. A. T. Winter, *Phil. Mag.*, 30, 1974, p. 719.
13. C. Laird, in *'Proc. A.S.M. Materials Science Seminar'*, St. Louis, Missouri, 1979, p. 149.
14. J. Botsis, A. Chudnovsky and A. Moet, *Int. J. Fracture,* 33, 1987, p. 263.
15. N. J. Mills and N. Walker, *J. Mater. Sci.,* 15, 1980, p. 1832.
16. M. E. Mackay, T. G. Teng and J. M. Schultz, *J. Mater. Sci.,* 14, 1979, p. 221.
17. M. Kitagawa, *J. Mater. Sci.,* 17, 1982, p. 2514.
18. J. Botsis, *J. Mater. Sci.,* 24, 1989, p. 2018.
19. A. Chudnovsky, *Crack Layer Theory*, 10th U. S. National Conference on Applied Mechanics, Ed. J. P. Lamb, ASME, Austin, Texas, 1986, p. 97.
20. J. Botsis, *Polymer*, 29, 1988, p. 457.
21. S. K. Aoki, Kishimoto and M. Sakata, *J. Appl. Mech.*, 48,1981, 825.
22. H. Tada, P. C. Paris and G. P. Irwin,*The Stress Analysis of Cracks Handbook*, Del Research Corp., Helertown Pennsylvania, 1975.
23. R. W. Hertzberg and J. A. Manson, *Fatigue in Engineering Plastics,* Academic Press, New York, 1980.
24. M. D. Skibo, R. W. Hertzberg and J. A. Manson, *J. Mater. Sci.,* 11, 1976, p. 479.
25. W. G. Knauss, in *'Advances in Fracture Research ICF7'*, eds K. Salama, K. Ravi-Chandar, D. M. R. Taplin and P. Rama Rao, Pergamon Press, N.Y. Vol. 4, p. 2683.
26. J. A. Sauer and G. C. Richardson, *Int. J. Fract.* 16, 1980, p. 499.
27. B. Gregory and J. Botsis, *J. Mater. Sci.,* 26, 1991, p. 1015.

APPENDIX I

Growth Behavior of the Gravity Center of a Core Zone Prior to Crack Initiation

The experimental results on the gravity center movements of a core zone before crack initiation are related with the corresponding energy release rate. A general outline of the method for evaluating energy release rates is given first and then the method is described when applied to a particular case.

A.1 The Double Layer Potential Technique

The stress field in an infinite linear elastic body containing an array of cracks (or crazes) with prescribed Mode I opening displacements can be calculated by the use of the second Green's tensor $\Phi_{ij}(x,x)$, for a unit discontinuity [A1]§ ,

$$\Phi_{ij} = -\frac{(1+v)}{4\pi R^2}\left[\frac{(1-v)}{(1+v)}(n_i R_j - n_j R_i + n_k R_k \delta_{ij}) + \frac{2n_k}{R^2}R_k R_i R_j\right] \tag{1}$$

Here v is the Poisson's ratio, $R_i = X_i - x_i$ and n_j stands for the unit normal on the discontinuity. The components of $\Phi_{ij}(x,x)$ render the displacement u_i at point x due to a unit discontinuity with unit normal n_j at point x (*Figure A.1a*).

It should be noted that although this function is recognized as the second Green's tensor which gives the traction response to a unit force it can be shown that it can also be applied for the displacement response due to a unit discontinuity.

The displacement response at point x due to a number of k discontinuities is given by the expression,

$$u_i(x) = \sum_{m=1}^{k}\int_{S_m} b_j^m(\xi)\,\Phi_{ij}(x,\xi)\,d\xi \tag{2}$$

where the sum is taken over all cracks and $b_j^m(x)$ is the opening of the mth crack at point x. The integration is performed along each crack line S_m (*Figure A.1b*) separately.

The stresses are given by the expression :

$$\sigma_{ij}(x) = \sum_{m=1}^{k}\int_{S_m} b^m(\xi)\,[\lambda\delta_{ij}\Phi_{lk,l} + \mu(\Phi_{ik,j} + \Phi_{jk,i})]\,n_k\,d\xi \tag{3}$$

Here $\Phi_{ij,m}$ is the derivative of Φ_{ij} with respect to x_m and is given by the following formula :

---

§ Symbols in brackets indicate cited literature at the end of the appendix

$$\Phi_{ij,m}=-\frac{(1+v)\,R_m}{2\pi R^4}\left[\frac{(1-v)}{(1+v)}(n_i R_j-n_j R_i+n_k R_k\delta_{ij})+\frac{2n_k}{R^2}R_k R_i R_j\right]$$

$$-\frac{(1+v)}{4\pi R^2}\left[\frac{(1-v)}{(1+v)}(n_j\delta_{im}-n_i\delta_{jm}-n_m\delta_{ij})-2n_m\frac{R_i}{R^2}R_j-2n_k R_k\delta_{im}\frac{R_j}{R^2}\right.$$

$$\left.+2n_k R_k R_i\left(-\frac{\delta_{jm}}{R^2}+\frac{2R_j}{R^4}R_m\right)\right]$$

Hence, knowledge of crack openings and their positions allows for the calculation of stresses and strains at any point within an infinite solid. Obviously, the shape of microcracks, their openings and positions may be assumed or be experimentally measured.

Application of the above method in a plate with defects would require that they are located at large distances from the plate edges. In the case where the defects are very close to the edges of the specimen the formalism of double layer as it is presented above can not be employed. This is because expression (1) is valid for an infinite solid. It can however, be implemented in the following superposition for the final solution of a finite solid with defects near its boundaries:

I.   The solution for the finite body without cracks which satisfies all the original boundary conditions.

II.   The solution for an infinite body containing the cracks with their prescribed openings. From this solution, the tractions and displacements along the boundaries of the finite body, if we imagine it as a part of the infinite one, can also be found.

III.   The solution for the finite body without cracks and loaded with tractions along the part of the boundary where tractions are prescribed and displacements along the part of the boundary where displacements are prescribed, opposite to those obtained from solution (II). A schematic of the three superimposing solutions for the case of a semi - infinite notched plate is shown in *Figure A.2*. Notice that solutions (I) and (III) can be combined into one.

A.2   Stress Analysis of a Single Edge Notched Strip

In this work, the above method was applied to a single edge notched specimen under plane stress conditions. An array of crazes was considered around the notch tip. The numerical scheme developed herein does not require any assumptions regarding the geometry of the notch or the configuration of the array of crazes. That is, the notch may be of any angle and the number and position of crazes can be arbitrary. The depth of the notch is only limited by the width of the strip.

It was assumed that the displacements of the craze boundaries can be measured experimentally. This information is sufficient to provide a solution to the problem under consideration.

From optical micrographs taken during the experiment, the openings of the arched crazes can be evaluated relatively easy. It was difficult however, to resolve openings of individual crazes within the core zone with available experimental techniques. What can be measured were approximate displacements caused by the core zone around its vicinity. Therefore, to evaluate the contribution of the core zone to the energy release rates we use displacements resulting from the core. Evidently, this is equivalent to segregating the core with an effective single discontinuity.

For the analysis of the experimental results and the evaluation of the energy release rates the following assumptions and simplifications were adopted:

i)   The tractions along the boundaries of the specimen, except along the V-notch, calculated by the double layer potential technique (part II), were taken negligible. This assumption was justified by the calculations using the particular specimen geometry and experimentally measured craze openings.

ii)   Only Mode I craze opening displacements were assumed for the calculations reported herein.

iii)   With reference to a coordinate system attached at the notch tip, the shape of the arched crazes was approximated by second degree polynomial (*Figure 2.2*);

$$\xi_2 = a_0 + a_1\xi_1 + a_2\xi_1^2$$

where a_0, a_1, and a_2 are constants which were evaluated for each crack separately by knowing the coordinates of three points on the crack line.

iv)   Craze openings were taken as:

$$b(s) = (b_0 + b_1 s + b_2 s^2 + b_3 s^3 + b_4 s^4)\sqrt{1 - (2s/s_{tot} - 1)^2} \qquad (4)$$

Here b_0, b_1, b_2, b_3, b_4 are all constants. They were evaluated for each crack by experimentally measuring its openings at five points. s is a length parameter along the crack and can be measured from either tip of the crack (*Figure A.1b*). In the case of a straight craze (or crack) expression (4) becomes Willis's fourth degree polynomial for crack opening [A2].

v)   The double layer potential technique requires that a great number of integrations be performed (Eqs. 2 and 3). Due to the complexity of the expressions involved these integrations cannot be performed analytically and a Gauss - Kronrod 20 - point numerical integration rule was employed.

vi)   A Finite Element Method program was developed to provide the numerical solution for the elastic fields in a V-notched strip loaded with tractions along its notch in addition to the remotely applied load. The program uses standard 8-node isoparametric quadrilaterals. The middle nodes of the elements surrounding the notch tip have been positioned at the one fourth of the side they belong to, so that those elements exhibit a $1/r^{0.5}$ singularity along their edges [A3]. This was only an approximation since the singularity of a 60° sharp notch is $1/r^{0.49}$ [A4].

A.3 Results and Discussion

The stresses and strains obtained from the method outlined in the preceding sections, were employed to evaluate the following two contour integrals;

$$J = \int_{C_1} (W n_i - T_k u_{k,i}) ds$$

$$M = \int_{C_2} (W x_i n_i - T_k u_{k,i} x_i) ds$$

where C_1, C_2 are closed contours of integration in the x_1, x_2 plane; W is the strain energy density; u_k is the displacement vector and T_k is the traction vector defined by the outward normal n_i to C_1 (C_2). Integrals J and M have been interpreted as the energy release rates due to translation and isotropic expansion of a cavity [A5]. The same interpretation holds true for a crack [A5] and a damage zone [A6,A7]. The contours of integration in the case of a straight crack in a plate is shown in *Figure A.3a*. Moreover, $J = J_1 - J_2$, where J_1 and J_2 are the values of the integral corresponding to extension of crack tip 1 and 2, respectively. It is important to notice at this point that the value of M integral is dependent on the coordinate system employed. Physically, the coordinate system should be taken at the center of isotropic expansion of a cavity or for that matter of a damage zone. Such data however, was not available. In this analysis, evaluation of the M integral was carried out with reference to a coordinate system attached at the notch tip.

The experimental results have shown two distinct damage patterns (*Figure A.2*); a core of intense craze zone and peripheral crazes. Accordingly, we evaluate the energy release rates for both these zones. The corresponding contours of integration are shown in *Figure A.3b*.

Values of J plotted against the number of cycles for the entire craze zone (a), peripheral crazes (b), and for the core (c) are displayed in *Figure A.4*. Notice that J is negative for the core zone and positive for the peripheral crazes. Moreover, in absolute values the contribution of the core was the largest which results in a negative overall value of J. The negative values of J can be explained on the basis that the core of crazes, considered as a single effective discontinuity, is embedded in a non homogeneous stress field (*Figure A.3c*). Thus $J_1 < J_2$ and $J = J_1 - J_2 < 0$. The continuous decrease in J was due to the fact that J_1 decreases and J_2 increases with damage growth.

The corresponding plots for M integral are shown in *Figure A.5*. Notice that M was positive for all three cases. It can also be seen that the peripheral crazes have an effect on the value of M integral for the core. Namely, the data suggests a shielding effect of the peripheral crazes on the core. Additional experimental and analytical work is needed to establish this effect.

The evolution of the total values of J and M approaches a plateau near crack initiation. If this trend was a result from the crack initiation event, it requires further experimental and analytical investigation.

The experimental data on craze growth and the corresponding values of the energy release rates can in principle be confronted as an attempt to assess their phenomenological relationships. Accordingly, J may be correlated with a kinetic parameter describing translation and M with one describing isotropic expansion. However, an accurate description of the kinetics of the core zone should result from analysis of craze distribution, within the zone at different times. In this analysis, the core zone was approximated by its length along the bisector of the V - notch (potential crack growth direction). Thus, a core speed can be correlated with J_c. This data is shown in *Figure A.6*. Note that the growth trend is similar to the growth of a fatigue crack.

On the other hand, the peripheral crazes were not straight. Thus, to correlate their gravity center kinematics two values of J are required. Due to limitations, however, on evaluating Mode II craze openings this task should await for improved experimental techniques to be developed.

It was stated earlier that the values of M depend on the coordinate system employed for its evaluation. In the present studies the coordinate system was taken at the notch tip. This may not be realistic to describe isotropic expansion of the core and of the peripheral crazes.

A1. A. Chudnovsky and M. Ben Onenzdou, *Int. J. Fract..*, 37, 1988, p. 3.

A2. J. R.Willis *Int. J. Eng. Sci.,* 6, 1968, p. 5.

A3. R. D.Cook, D. S. Malkus and M. E. Plesha, *Consepts and Applications of Finite Element Analysis*, (3rd Edn)., John Wiley, N.Y. 1989.

A4. K. Y. Lin and P. Tong, *Int. J. Numr Meth. Engr.*, 15, 1980, p. 1343

A5. B. Budiansky and J. R. Rice, *J. Appl. Mech.*, 40, 1973, p. 201.

A6. A. Chudnovsky, *Crack Layer Theory*, 10th U. S. National Conference on Applied Mechanics, Ed. J. P. Lamb, ASME Austin, Texas, 1986, p. 97.

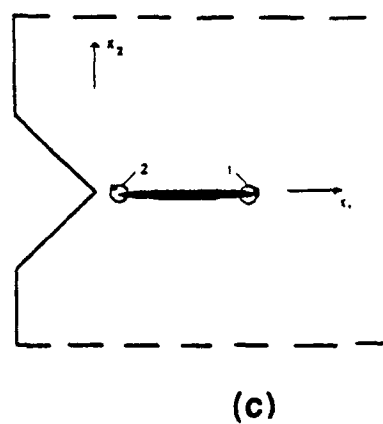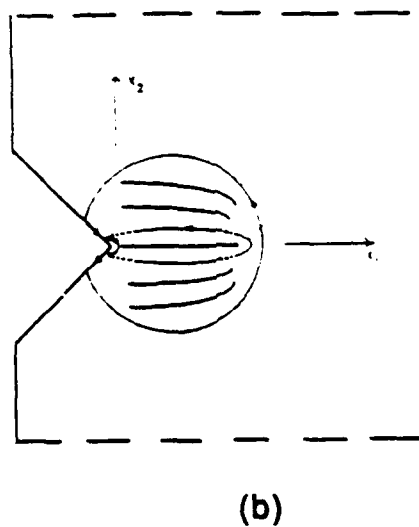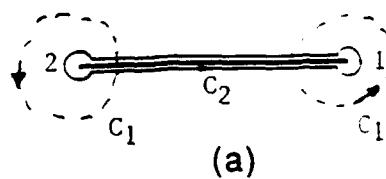A7. S. K. Aoki, Kishimoto and M. Sakata, *J. Appl. Mech.*, 48, 1981, 825.
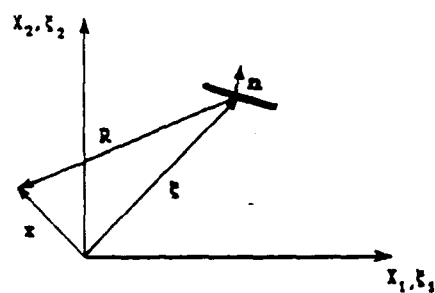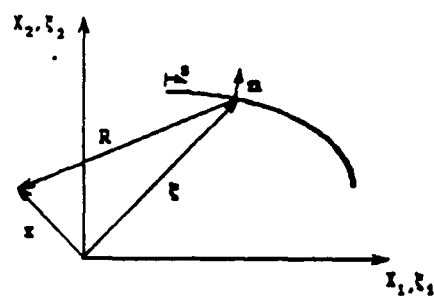
Figure A.1   Illustration of displacement response at point **x**, given by expression (1); (a) due to a unit discontinuity at point **x**; (b) due to a crack

V-notched plate without damage. Method of solution: FEM

(I)

Infinite body with damage. Method of solution: Double layer Potential

pseudotractions along α·n

(II)

V-notched plate loaded with tractions along V-notch. Method of solution: F.E.M.

(III)

X_1

X_2

Figure A.2   Schematic of the superposition principle applied to evaluate J and M integrals

(a)

(b)

(c)

Figure A.3 Contours of integration for M and J integrals: (a) for a straight crack, (b) for a V- notch surrounded by damage, (c) Effective discontinuity in a non - homogeneous stress field
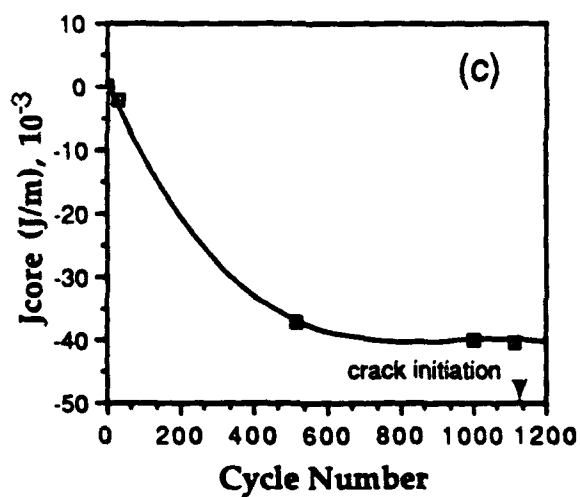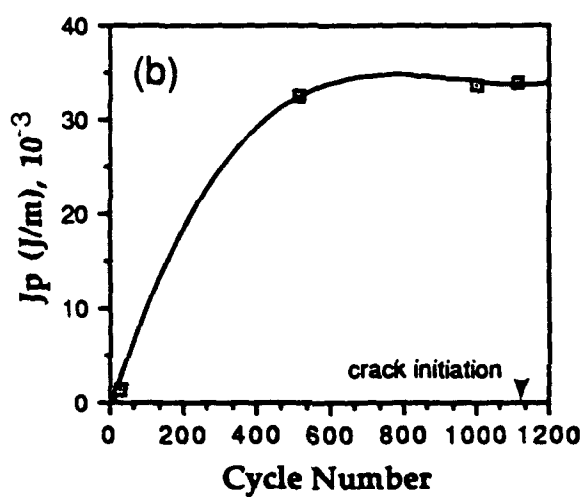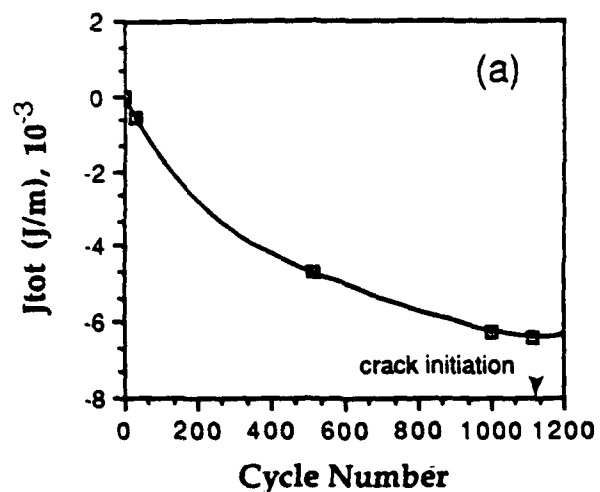
Figure A.4   Results of J evaluation for (a) entire craze zone, (b) peripheral crazes, (c) core crazes
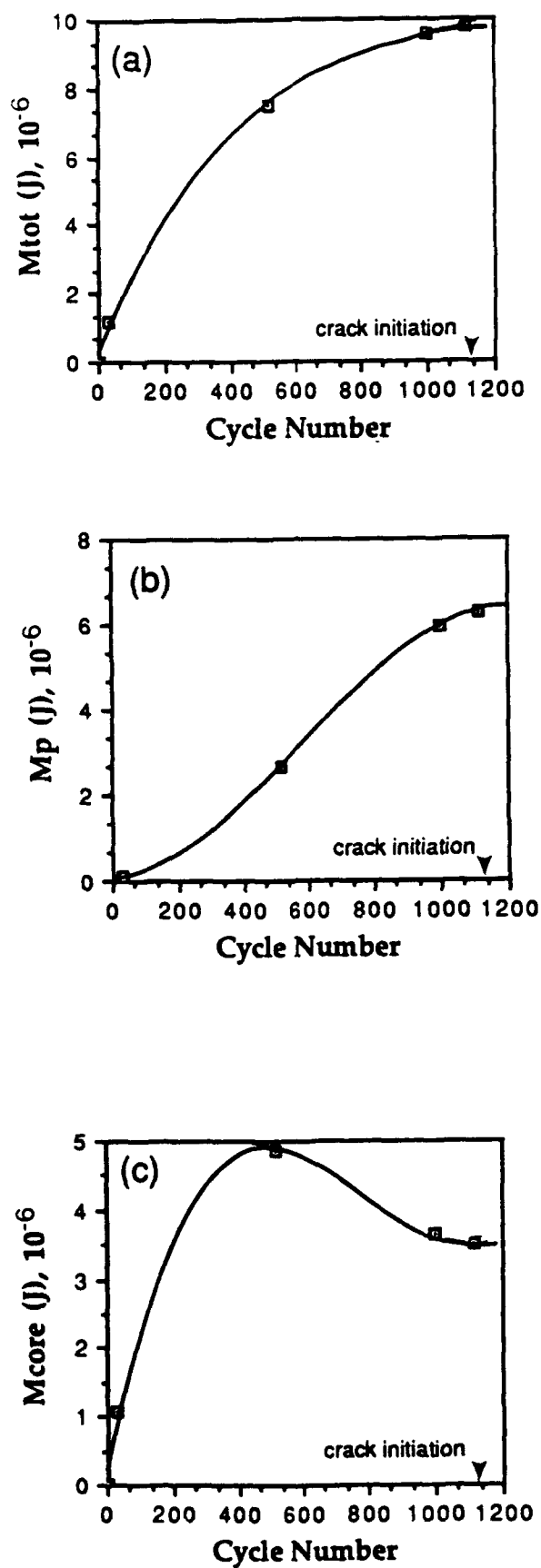
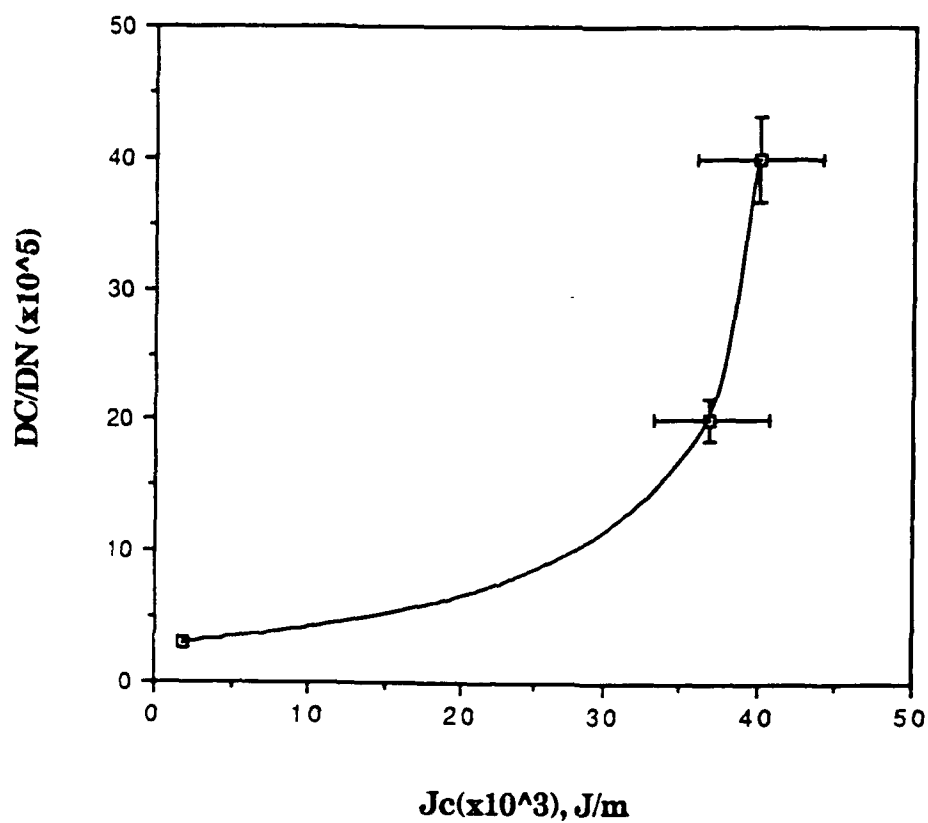*Figure A.5* Results of M evaluation for: (a) entire craze zone, (b) peripheral crazes, (c) core crazes

Figure A.6   Evolution of Core Zone Speed with Energy Release Rate|Jc|

LIST OF PROFESSIONAL PERSONEL AND PUBLICATIONS

Personel:

- J. Botsis, Associate Professor

- X. Q. Zhang, Ph. D. Completed, Spring, 1991.

- C. Huang, Ph. D. Expected Graduation Fall 1992 (Partial Participation in this work).

Publications:

1. B. L. Gregory and J. Botsis, 'Experimental Investigation of the Effects of Stress Rate and Stress Level on Fracture in Polystyrene', *Journal of Materials Science,* 26, 1991, p. 1015.

2. J. Botsis and X. Q. Zhang, 'On the Kinematics of Damage Evolution During Fatigue Fracture', *Journal of Materials Science,* 26, 1991, p. 1421.

3. C. Huang and J. Botsis, 'Experimental Studies in Crack Initiation', *Symposium on the Promotion of the Application of Local Fracture/Damage models to Engineering Fracture Problems,* ASME Summer Meeting, AMD, Vol. 137, 1992, p. 131.

4. C. Huang and J. Botsis, 'Damage Evolution During Crack Initiation Under Fatigue', in preparation, to be Submitted in the *Journal of Materials Science,* Summer, 1992.

REPORT DOCUMENTATION PAGE

1a. REPORT SECURITY CLASSIFICATION	1b. RESTRICTIVE MARKINGS
Unclassified	

2a. SECURITY CLASSIFICATION AUTHORITY	3. DISTRIBUTION/AVAILABILITY OF REPORT
	Approved for public release;
2b. DECLASSIFICATION / DOWNGRADING SCHEDULE	distribution unlimited

4. PERFORMING ORGANIZATION REPORT NUMBER(S)	5. MONITORING ORGANIZATION REPORT NUMBER(S)

6a. NAME OF PERFORMING ORGANIZATION	6b. OFFICE SYMBOL (If applicable)	7a. NAME OF MONITORING ORGANIZATION
University of Illinois Chicago		AFOSR

6c. ADDRESS (City, State, and ZIP Code)	7b. ADDRESS (City, State, and ZIP Code)
Department of Civil Engineering Mechanics & Metallurgy, ERF 2081 Box 4348, Chicago, IL 60630	Same as 8 c.

8a. NAME OF FUNDING/SPONSORING ORGANIZATION	8b. OFFICE SYMBOL (If applicable)	9. PROCUREMENT INSTRUMENT IDENTIFICATION NUMBER
Aerospace Sciences/AFOSR	NA	91-0505 AFOSR-88-0104

8c. ADDRESS (City, State, and ZIP Code)	10. SOURCE OF FUNDING NUMBERS			
	PROGRAM ELEMENT NO.	PROJECT NO.	TASK NO.	WORK UNIT ACCESSION NO.
Bolling, ABF AFB Washington, D.C. 20332 - 6448	61102F	2302	BS	

11. TITLE (Include Security Classification)
Experimental and Analytical Studies on
the Kinematics of Damage Zone During Fatigue Fracture (u)

12. PERSONAL AUTHOR(S)
John Botsis

13a. TYPE OF REPORT	13b. TIME COVERED	14. DATE OF REPORT (Year, Month, Day)	15. PAGE COUNT
FINAL	FROM 9/89 TO 4/92		

16. SUPPLEMENTARY NOTATION

17.	COSATI CODES		18. SUBJECT TERMS (Continue on reverse if necessary and identify by block number)
FIELD	GROUP	SUB-GROUP	Crack Initiation, Crack Propagation, Damage, Process Zone
			Affine Transformation, Energy Release Rate.

19. ABSTRACT (Continue on reverse if necessary and identify by block number)

This report provides a summary of the results obtained in a research program on damage evolution before crack initiation and during slow crack propagation on a model material. First the main results on crack initiation are given. Subsequently, damage evolution within a process zone is described in some details. Results of the effects of stress rate and stress level on crack damage evolution is presented next. In appendix A, an approximate method to evaluate energy release rates due to damage growth is applied using the data on crack initiation.

20. DISTRIBUTION/AVAILABILITY OF ABSTRACT	21. ABSTRACT SECURITY CLASSIFICATION
☐ UNCLASSIFIED/UNLIMITED ☐ SAME AS RPT ☑ DTIC USERS	(u)

22a. NAME OF RESPONSIBLE INDIVIDUAL	22b. TELEPHONE (Include Area Code)	22c. OFFICE SYMBOL
Dr. Walter F. Jones	(202) 767-4970	NA